Exergy Balance Extension to Rotating Reference Frames: Application to a Propeller Configuration

Ilyès Berhouni, Didier Bailly, Ilias Petropoulos

Exergy Balance Extension to Rotating Reference Frames: Application to a Propeller Configuration

Ilyès Berhouni*, Didier Bailly†, Ilias Petropoulos‡
ONERA - The French Aerospace Lab, Meudon, F-92190, France

The exergy analysis has already proved to be of interest for aerospace applications, with the possibility to analyze new types of configurations. It is of particular interest when a pertinent thrust/drag breakdown is not possible and when significant thermal exchanges take place in the control volume. In addition, this method allows to link the different contributions of the exergy terms to physical phenomena in the flow, improving the understanding of the sources of losses degrading the performance of the system under study. The applications and results obtained in a fixed frame of reference have thus motivated the improvement and extension of the exergy balance to more complex flows. This paper aims at presenting an extension of the exergy balance to rotating frames of reference for the analysis of rotating components of the propulsion system (e.g. propeller, turbomachine or helicopter rotor blades). The newly developed theoretical development is summarized, and an application to a numerical simulation of a propeller is presented. Results are discussed both in terms of physical interpretation and numerical accuracy.

I. Nomenclature

$\dot{A}$	=	Entropy outflow through S_o, J.s^{-1}
$\dot{A}_{sp}$	=	Spurious anergy generation, J.s^{-1}
$\dot{\mathcal{A}}_{tot}$	=	$\dot{\mathcal{A}}_\phi + \dot{\mathcal{A}}_{\nabla T} + \dot{\mathcal{A}}_w$, Rate of total anergy generation, J.s^{-1}
$\dot{\mathcal{A}}_w$	=	Rate of anergy generation by shockwaves, J.s^{-1}
$\dot{\mathcal{A}}_{\nabla T}$	=	Rate of anergy generation by thermal mixing, J.s^{-1}
$\dot{\mathcal{A}}_\phi$	=	Rate of anergy generation by viscous dissipation, J.s^{-1}
$\boldsymbol{C}$	=	Transformation matrix between a fixed and a rotating frame
C_p	=	$\frac{p-p_\infty}{0.5\rho_\infty V_\infty^2}$, Pressure coefficient
c_p	=	Specific heat capacity at constant pressure, J.K^{-1}.kg^{-1}

Presented as Paper 2022-0298 at the AIAA SciTech 2022 Forum, San Diego, CA & Virtual, 3-7 January 2022.
*Ph.D. student, ONERA Department of Aerodynamics, Aeroelasticity, Acoustics, ilyes.berhouni@onera.fr.
†Research Scientist, Ph.D., ONERA Department of Aerodynamics, Aeroelasticity, Acoustics, didier.bailly@onera.fr.
‡Research Scientist, Ph.D., ONERA Department of Aerodynamics, Aeroelasticity, Acoustics, ilias.petropoulos@onera.fr.

E = Mass-specific total energy, J.kg^{-1}

$E^*, A^*, \dot{\mathcal{X}}^*$ = Numerical precision indicators

EWC = Exergy-Waste Coefficient

$\dot{E}_m$ = Mechanical energy outflow, J.s^{-1}

$\dot{E}_u$ = Streamwise kinetic energy outflow, J.s^{-1}

$\dot{E}_{vw}$ = Transverse kinetic energy outflow, J.s^{-1}

$\dot{E}_p$ = Boundary pressure-work rate, J.s^{-1}

$\dot{E}_{th}$ = Rate of thermal energy outflow, J.s^{-1}

$\dot{E}_W$ = Boundary isobaric pressure-work rate, J.s^{-1}

e = Mass-specific internal energy, J.kg^{-1}

F_X = Axial force, N

H = Mass-specific total enthalpy, J.kg^{-1}

h = Mass-specific enthalpy, J.kg^{-1}

$\overline{\overline{I}}$ = Identity tensor

J = $\frac{V_\infty}{2r_p N}$, Propeller advance ratio

k = Thermal conductivity, W.m^{-1}.K^{-1}

k_{eff} = $c_p \left(\frac{\mu_l}{Pr} + \frac{\mu_t}{Pr_t} \right)$, Effective thermal conductivity, W.m^{-1}.K^{-1}

M = Mach number

N = $\frac{\omega}{2\pi}$ Angular velocity in rotations per second

$\mathbf{n}$ = Unit normal vector

Pr = Prandtl-number

Pr_t = Turbulent Prandtl-number

p = Static pressure, kg.m.s^{-2}

pc = Power counts (10^{-4})

$\mathbf{q}$ = Heat flux by conduction, J.s^{-1}

$\mathbf{q}_{eff}$ = $-k_{eff}\nabla\mathbf{T}$, Effective heat flux by conduction, J.s^{-1}

R_f = Inertial fixed reference frame

R_r = Non-inertial rotating reference frame

Re = Reynolds number

$\mathbf{r}$ = Position vector

r_p = Propeller radius, m

$\overline{\overline{S}}$ = Strain rate, s^{-1}

S_b = Body surface

S_o = Outer boundary of the control volume

S_{ref} = Reference surface, m^2

S_w = Shockwave surface

s = Mass-specific entropy, $J.K^{-1}.kg^{-1}$

$\mathbf{s_e}$ = $\omega \times \mathbf{r}$, Rotating velocity, $m.s^{-1}$

T = Static temperature, K

T_X = Axial torque, N.m

$\mathcal{V}$ = Control volume

$\mathbf{V}$ = $(V_\infty + u)\mathbf{x}, v\mathbf{y}, w\mathbf{z}$, Fluid velocity vector, $m.s^{-1}$

$\mathbf{V}_r$ = $\mathbf{V} - \mathbf{s_e}$, relative velocity, $m.s^{-1}$

$W\dot{\Gamma}$ = Power consumed by the body to maintain its current axial equilibrium, $J.s^{-1}$

$\dot{\mathcal{X}}_m$ = Rate of mechanical exergy outflow, $J.s^{-1}$

$\dot{\mathcal{X}}_{qb}$ = Rate of thermal exergy supplied by conduction through S_b, $J.s^{-1}$

$\dot{\mathcal{X}}_{qo}$ = Rate of thermal exergy supplied by conduction through S_o, $J.s^{-1}$

$\dot{\mathcal{X}}_r$ = Power transferred from the solid body to the flow through the torque, $J.s^{-1}$

$\dot{\mathcal{X}}_{th}$ = Rate of thermal exergy outflow, $J.s^{-1}$

χ = Mass-specific exergy, $J.kg^{-1}$

χ_f = Mass-specific flow exergy, $J.kg^{-1}$

x_{TP} = Transverse plane x-coordinate, m

α_r = Relative angle of attack

$\delta(\ )$ = Perturbation of a quantity relative to the freestream, $= (\ ) - (\ )_\infty$

μ = Fluid dynamic viscosity, $kg.m.s^{-1}$

μ_l = Fluid laminar dynamic viscosity, $kg.m.s^{-1}$

μ_t = Fluid turbulent dynamic viscosity, $kg.m.s^{-1}$

ρ = Density, $kg.m^{-3}$

$\overline{\overline{\tau}}$ = Viscous stress tensor, N

$\overline{\overline{\tau}}_{eff}$ = $(\mu_l + \mu_t)\overline{\overline{S}}$, Effective viscous stress tensor, N

τ_o = Rate of work of the viscous force on S_o linked to velocity perturbations, $J.s^{-1}$

ψ_p = Effective propulsive efficiency

ψ_{pr} = Reversible effective efficiency

ϕ = Dissipation rate per unit volume, $J.s^{-1}.m^{-3}$

ϕ_{eff} = $(\overline{\overline{\tau}}_{eff} \cdot \nabla) \cdot \mathbf{V}$, Effective dissipation rate per unit volume, J.s^{-1}.m^{-3}

$\boldsymbol{\omega}$ = Angular velocity, rad.s^{-1}

$(\,)_{,nf}$ = Quantity $(\,)$ computed with its near-field expression

$(\,)_{\infty}$ = Quantity $(\,)$ at freestream conditions

$(\,)'$ = Quantity $(\,)$ projected in the relative frame, = $\boldsymbol{C}^T(\,)$

∇ = Nabla operator

$:=$ = Equal by definition

$[\![\ ]\!]$ = Discontinuous jump of a quantity

$\frac{d}{dt}_{\mathbf{s_e}}$ = Material derivative of a quantity expressed in the velocity field $\mathbf{s_e}$

II. Introduction

Ever since the first commercial flights, the search for better aircraft efficiency has been a leading factor that motivated the evolution of aircraft. The reduction of the environmental footprint has since then become a significant goal for the civil aircraft industry. Due to the raising objectives for the reduction of greenhouse gas emissions which came with stimulus plans, the aviation sector has to keep evolving faster in order to reach better results in terms of pollutant emissions. Such rapid improvements imply the development of disruptive technologies [1, 2], as this gain of efficiency must come from all areas of development of aircraft, such as the external aerodynamic efficiency, the source of energy and the effectiveness of the propulsion systems.

In this context, new configurations allowing a better aerodynamic efficiency like the Boundary Layer Ingestion (BLI) or the Unducted Single Fan (USF) concepts, among others, are considered to be promising. To analyze the performance of new-generation configurations where the separation between thrust and drag is not as obvious as for a tube-and-wing architecture, the need for new theoretical and numerical models has emerged. Indeed, classical force-based models evaluating the different drag components [3–5] are less adapted to evaluate the performance of such new concepts. Adaptations of these models are thus required, yet the absence of a rigorous definition for force components does not allow a completely objective validation of such modifications [6]. In order to tackle this problem, a novel approach based on a mechanical energy analysis for transonic to supersonic aircraft was proposed by Drela [7]. This approach avoids the need for a thrust/drag separation that appears with force-based analyses, and still allows a pertinent quantification of the influence of the different phenomena in the flow that are of interest in the process of designing an aircraft, such as shockwaves, wakes and lift-induced vortices. The physical interpretation of the power balance method has since been further studied [8] and applied to the performance investigation of the BLI concept [8–10].

The power balance approach of Drela allows to study new configurations such as BLI from a mechanical point of view, but does not take into account thermal effects. This motivated the development of another approach at ONERA

based on the concept of exergy [11], which corresponds to the maximum theoretical work that can be extracted from the system under study, thermal or mechanical. The interest for the use of exergy in the field of aerospace engineering has grown over the last decades, with an example being the introduction of exergy analysis applied to aerospace vehicle design by Moorhouse and Camberos [12, 13]. A formulation based on an exergy balance adapted to external aerodynamics analysis was later developed by Arntz et al. [14, 15] and allowed to link the different components of the exergy balance to reversible and irreversible physical phenomena. This formulation was successfully applied to conventional and disruptive configurations of aircraft [15], as well as studied and improved numerically [16] over the last years. Other works have been performed recently to use this exergy balance in the frame of various numerical and experimental applications [17–19], such as adaptations aiming at estimating an exergy-based drag coefficient in wind-tunnel applications.

The most recent exergy balance formulation to date can be applied to aircraft configurations in a fixed reference frame, but does not sufficiently cover rotating configurations. The special case of rotating frames of reference is of interest when considering turbomachines, propellers or turbofans, as the exergy balance could be used to localize sources of loss with the goal to optimize such configurations. The benefits of the exergy concept are even greater for configurations with significant thermal exchanges, as this aspect is not adequately captured by force-based approaches.

An exergy balance adapted to such cases was investigated by Fiore [20] and applied to a linear cascade composed of five nozzle guide vanes, and to a two-stage rotating turbine configuration. However, the equations were not written in their arbitrary Lagrangian-Eulerian form and the final decomposition did not let the momentum conservation equation appear explicitly either. As a consequence, the inertial terms appearing for a rotating frame of reference could not appear explicitly either. Furthermore, the absence of the use of the momentum equation does not allow to explicitely describe the power consumed to maintain the current axial equilibrium (which can be further linked to drag and thrust). The point of view adopted was thus different than the one used by Arntz: the latest gives a clearer link between far-field terms of the final exergy balance and physical phenomena appearing in the near-field.

This paper aims at presenting the development of the exergy balance for rotating reference frames and its application to a propeller configuration with the post-processing code FFX (Far-Field eXergy) developed and used at ONERA. The theoretical derivation is detailed in Sec. III, and results highlighting the interest of the exergy balance in the case of a propeller analysis are presented in Sec. IV. A conclusion on the results obtained and perspectives on this work are presented in Sec. V.

III. Exergy balance for rotating frames of reference

A. System definition

The fluid flow analysis is carried out in a continuous volume $\mathcal{V}$ delimited by a solid body surface S_b and an outer boundary S_o, as illustrated in Fig. 1. The control volume follows the movement of the body which is in rotation at a velocity $\mathbf{s_e}$ with respect to the inertial fixed frame R_f, and a non-inertial relative frame R_r is attached to it. The rotating velocity is expressed as $\mathbf{s_e} = \boldsymbol{\omega} \times \mathbf{r}$, where $\boldsymbol{\omega}$ is the angular velocity, considered constant both in amplitude and direction. A vector pointing outwards of the volume and locally normal to the surface is noted $\mathbf{n}$. Since the volume follows the movement of the body with the same velocity $\mathbf{s_e}$, a steady-state assumption is considered in the relative frame. The presence of a steady shockwave attached to the body is also considered through a surface of discontinuity S_w.

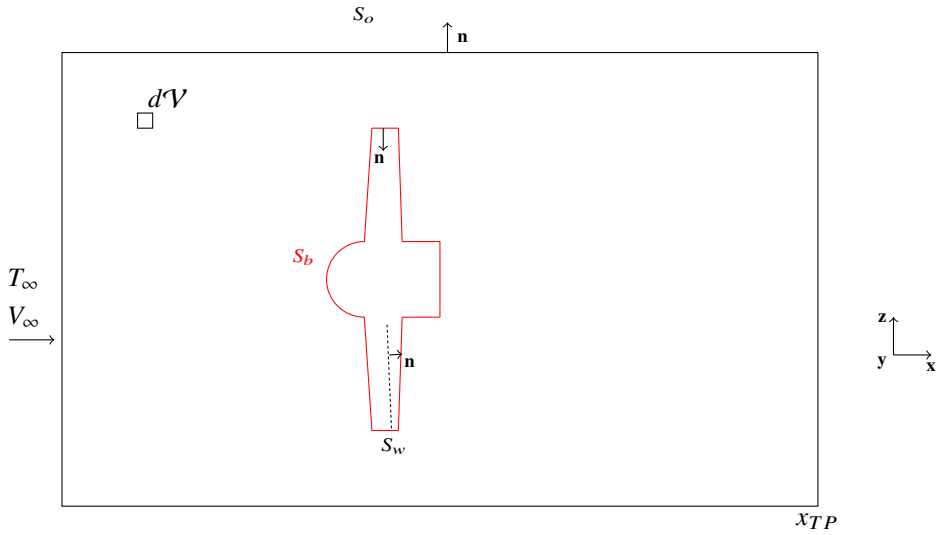

Fig. 1 2D cross section of a 3D control volume surrounding a solid body in rotation.

The system is thermodynamically open as it can exchange mass, work and heat with the surrounding fluid across its boundaries. The atmosphere is considered as a thermal and mechanical reservoir surrounding the control volume, and also corresponds to the reference (or dead) state in the exergy definition that is detailed in a further section. The analysis is carried out in the reference frame R_r, which is non-inertial, and the control volume is therefore fixed in the rotating frame of reference with the air flowing in and out of it. In Fig. 1, the near-field surface has been chosen as the rotating body's surface, giving the null relative velocity as the wall condition on S_b, i.e. $(\mathbf{V}' - \mathbf{s_e}') = \mathbf{0}$ where the superscript $'$ indicates that the quantities are projected on the rotating frame. The control volume extends up to a transverse plane placed at a fixed coordinate x_{TP}.

Four hypotheses are made in the rest of this paper:

- The air is considered a perfect gas.
- The flow is steady in the rotating reference frame R_r.

- $\boldsymbol{\omega} = (\omega, 0, 0)^T$, i.e. the angular velocity is constant and oriented along the **x** axis.
- $\mathbf{V}' = (V'_\infty + u', v', w')^T$, i.e. the reference state velocity is defined along the rotation axis and the velocity perturbations in the rotating frame of reference are noted u',v' and w'.

B. Equations of interest expressed in the rotating frame of reference

1. Choice of the formulation

When writing the equations of fluid dynamics in a rotating frame of reference, there are several possibilities. In this case, the goal is to be able to consider the system as steady in R_r with the corresponding simplifications for the equations, which is achieved by writing the equations in the Arbitrary Lagrangian-Eulerian (ALE) form. Two well-known possibilities considered for this study are well detailed by Boniface [21] and Kozuch [22]: for both options, all quantities are projected in the relative frame, but then the equations can be written either as functions of the absolute velocity or as functions of the relative velocity. These two formulations are strictly equivalent, but allow to describe the physics of the flow from a different perspective. The mesh coordinates are projected in the rotating reference frame in both cases, the difference then consisting in either describing the flow with projected quantities from the fixed reference frame (absolute velocity formulation) or from the relative one (relative velocity).

In this paper, the first formulation is selected and is referred to as the absolute velocity, relative frame (noted AVRF) formulation. The exergy balance and all the equations used in its derivation are hence written in their AVRF form in the next sections.

2. Conservation equations in a rotating frame of reference

With the steady-state assumption in the rotating reference frame, the mass, momentum and energy integral equations are written in their AVRF form:

$$\int_{\partial\mathcal{V}} \rho(\mathbf{V}' - \mathbf{s_e}') \cdot \mathbf{n}' \, \mathrm{d}S = 0 \tag{1}$$

$$\boldsymbol{\omega}' \times \int_{\mathcal{V}} \rho \mathbf{V}' \, \mathrm{d}\mathcal{V} + \int_{\partial\mathcal{V}} (\rho \mathbf{V}' \otimes (\mathbf{V}' - \mathbf{s_e}') + (p\overline{\overline{I}}' - \overline{\overline{\tau}}')) \cdot \mathbf{n}' \, \mathrm{d}S = \mathbf{0} \tag{2}$$

$$\int_{\partial\mathcal{V}} (\rho\delta E(\mathbf{V}' - \mathbf{s_e}') + \mathbf{q}' + (p\overline{\overline{I}}' - \overline{\overline{\tau}}') \cdot \mathbf{V}') \cdot \mathbf{n}' \, \mathrm{d}S = 0 \tag{3}$$

The mass and energy conservation equations are very similar to those expressed in the fixed reference frame, with the only difference being that the relative velocity $(\mathbf{V}' - \mathbf{s_e}')$ appears in the mass and energy flow terms. This remains true for the momentum equation, but, as it is a vector equation, an inertial term $\boldsymbol{\omega}' \times \int_{\mathcal{V}} \rho \mathbf{V}' \, \mathrm{d}\mathcal{V}$ is also included. These

equations hold when a discontinuity is considered in the control volume with the compatibility relations:

$$\begin{cases} [\![\rho(\mathbf{V}' - \mathbf{s_e}')]\!] \cdot \mathbf{n}' = 0 & (4) \\ [\![\rho \mathbf{V}' \otimes (\mathbf{V}' - \mathbf{s_e}') + p\overline{\overline{I}}' - \overline{\overline{\tau}}']\!] \cdot \mathbf{n}' = \mathbf{0} & (5) \\ [\![\rho E(\mathbf{V}' - \mathbf{s_e}') + \mathbf{q}' + (p\overline{\overline{I}}' - \overline{\overline{\tau}}') \cdot \mathbf{V}']\!] \cdot \mathbf{n}' = 0 & (6) \end{cases}$$

By doing the scalar product between $\mathbf{V}'_\infty$ and Eq. (2), a first quantity is introduced:

$$\begin{aligned} W\dot{\Gamma}' &= \int_{S_o} (\rho u' V'_\infty (\mathbf{V}' - \mathbf{s_e}') + (p - p_\infty)\mathbf{V}'_\infty - (\overline{\overline{\tau}}' \cdot \mathbf{V}'_\infty)) \cdot \mathbf{n}' \, \mathrm{d}S + \mathbf{V}'_\infty \cdot \cancel{\int_{\mathcal{V}} \rho \boldsymbol{\omega}' \times \mathbf{V}' \, \mathrm{d}\mathcal{V}} \\ &= -\int_{S_b} ((p - p_\infty)\mathbf{V}'_\infty - (\overline{\overline{\tau}}' \cdot \mathbf{V}'_\infty)) \cdot \mathbf{n}' \, \mathrm{d}S \end{aligned}$$

which is the power consumed by the body to maintain its current axial equilibrium. The second term of this equation is cancelled due to the reference velocity being parallel to the axis of rotation, but its value should be evaluated otherwise.

In addition to these equations, the torque conservation equation is considered in its integral form:

$$\int_{\partial\mathcal{V}} ((\mathbf{r} \times \rho\mathbf{V})'(\mathbf{V}' - \mathbf{s_e}') + (\mathbf{r} \times ((p - p_\infty)\overline{\overline{I}} - \overline{\overline{\tau}}))') \cdot \mathbf{n}' \, \mathrm{d}S + \boldsymbol{\omega}' \times \int_{\mathcal{V}} (\mathbf{r} \times \rho\mathbf{V})' \, \mathrm{d}\mathcal{V} = \mathbf{0} \tag{7}$$

The power transmitted from the solid body to the flow through the torque is then introduced by its scalar product with $\boldsymbol{\omega}'$:

$$\begin{aligned} \dot{\mathcal{X}}'_r &= \int_{S_o} (\rho(\mathbf{V}' \cdot \mathbf{s_e}')(\mathbf{V}' - \mathbf{s_e}') \cdot \mathbf{n}' + (p - p_\infty)(\mathbf{s_e}' \cdot \mathbf{n}') - (\overline{\overline{\tau}}' \cdot \mathbf{s_e}') \cdot \mathbf{n}') \, \mathrm{d}S \\ &= -\int_{S_b} ((p - p_\infty)(\mathbf{s_e}' \cdot \mathbf{n}') - (\overline{\overline{\tau}}' \cdot \mathbf{s_e}') \cdot \mathbf{n}') \, \mathrm{d}S \end{aligned}$$

In the rest of this paper, the integral expressions computed on S_o are referred to as far-field expressions, with the corresponding notations $W\dot{\Gamma}'$ and $\dot{\mathcal{X}}'_r$. The ones calculated on S_b are mentioned as near-field expressions and the corresponding results are noted $W\dot{\Gamma}'_{,nf}$ and $\dot{\mathcal{X}}'_{r,nf}$. The difference observed between the numerical results obtained using near-field or far-field expressions is discussed in Appendix A.

3. Second law of thermodynamics

The entropy equation multiplied by T_∞ in its integral form (corresponding to the second law of thermodynamics) is considered, as:

$$-T_\infty \int_{\partial\mathcal{V}} \rho\delta s(\mathbf{V}' - \mathbf{s_e}') \cdot \mathbf{n}' \, \mathrm{d}S - \int_{\partial\mathcal{V}} \frac{T_\infty}{T}\mathbf{q}' \cdot \mathbf{n}' \, \mathrm{d}S + \int_{\mathcal{V}} \frac{T_\infty}{T^2} k(\nabla T)'^2 \, \mathrm{d}\mathcal{V} + \int_{\mathcal{V}} \frac{T_\infty}{T}\phi' \, \mathrm{d}\mathcal{V} + \int_{S_w} [\![\frac{T_\infty}{T}\mathbf{q}' + T_\infty\rho\delta s(\mathbf{V}' - \mathbf{s_e}')]\!] \cdot \mathbf{n}' \, \mathrm{d}S = 0 \quad (8)$$

where $\phi' = (\overline{\overline{\tau}}' \cdot \nabla') \cdot \mathbf{V}'$ is the dissipation rate per unit volume corresponding to viscous phenomena inside the control volume, and $\mathbf{q}' = -k(\nabla T)'$ corresponds to the Fourier law.

4. Exergy balance

Exergy is defined as the maximum theoretically recoverable work with respect to a reference state. When considering a perfect gas at rest and neglecting the gravitational potential energy, the specific exergy is:

$$\chi = \delta E + p_\infty \delta\left(\frac{1}{\rho}\right) - T_\infty \delta s \quad (9)$$

When considering a flowing fluid, the flow specific exergy definition is slightly different due to the consideration of the pressure forces driving the flow, as well as the kinetic energy [11]. The specific flow exergy is expressed mathematically for an open system as:

$$\chi_f = \delta H - T_\infty \delta s \quad (10)$$

Both definitions describe the same principle: the recoverable energy that can be extracted from a system corresponds to the part of the energy that is not destroyed by irreversible phenomena, which are linked to entropy production. From this, the exergy balance equation can be written in the rotating frame as:

$$\frac{d}{dt}_{\mathbf{s_e}} \int_{\mathcal{V}} \rho\chi \, \mathrm{d}\mathcal{V} + \int_{\partial\mathcal{V}} \rho\chi(\mathbf{V}' - \mathbf{s_e}') \cdot \mathbf{n}' \, \mathrm{d}S = \frac{d}{dt}_{\mathbf{s_e}} \int_{\mathcal{V}} \rho(\delta E + p_\infty \delta\left(\frac{1}{\rho}\right) - T_\infty\delta s) \, \mathrm{d}\mathcal{V} + \int_{\partial\mathcal{V}} \rho(\delta E + p_\infty \delta\left(\frac{1}{\rho}\right) - T_\infty\delta s)(\mathbf{V}' - \mathbf{s_e}') \cdot \mathbf{n}' \, \mathrm{d}S \quad (11)$$

Which can be simplified in the steady case as:

$$\int_{\partial\mathcal{V}} \rho\chi(\mathbf{V}' - \mathbf{s_e}') \cdot \mathbf{n}' \, \mathrm{d}S = \int_{\partial\mathcal{V}} \rho(\delta E + p_\infty \delta\left(\frac{1}{\rho}\right) - T_\infty\delta s)(\mathbf{V}' - \mathbf{s_e}') \cdot \mathbf{n}' \, \mathrm{d}S \quad (12)$$

5. Final steady exergy balance in its AVRF form

By injecting Eqs. (3) and (8) into Eq. (12), the steady exergy balance expressed in the rotating frame of reference is obtained:

$$\dot{\mathcal{X}}'_{qb} + \dot{\mathcal{X}}'_{r} = W\dot{\Gamma}' + \dot{\mathcal{X}}'_{m} + \dot{\mathcal{X}}'_{th} + \dot{\mathcal{A}}'_{\phi} + \dot{\mathcal{A}}'_{\nabla T} + \dot{\mathcal{A}}'_{w} + \tau'_{o} - \dot{\mathcal{X}}'_{qo} \tag{13}$$

from which several terms are defined:

- $\dot{\mathcal{X}}'_{qb} := -\int_{S_b} \left(1 - \frac{T_\infty}{T}\right) \mathbf{q}' \cdot \mathbf{n}' \, \mathrm{d}S$ is the rate of exergy supplied by thermal conduction through non-adiabatic walls on S_b. The sum of this term and $\dot{\mathcal{X}}'_{r}$ corresponds to the total rate of exergy supplied to the system in the absence of throughflow surfaces on S_b.

- $\dot{\mathcal{X}}'_{m} := \underbrace{\int_{S_o} \frac{1}{2}\rho u'^2 (\mathbf{V}' - \mathbf{s_e}') \cdot \mathbf{n}' \, \mathrm{d}S}_{\dot{E}'_u} + \underbrace{\int_{S_o} \frac{1}{2}\rho (v'^2 + w'^2)(\mathbf{V}' - \mathbf{s_e}') \cdot \mathbf{n}' \, \mathrm{d}S}_{\dot{E}'_{vw}} + \underbrace{\int_{S_o} (p - p_\infty)(\mathbf{V}' - \mathbf{V}'_\infty) \cdot \mathbf{n}' \, \mathrm{d}S}_{\dot{E}'_p}$ is the mechanical exergy wasted, as it leaves the control volume without being used. It is composed of three terms which correspond respectively to the longitudinal kinetic perturbation energy associated to wakes or jets, the transversal kinetic perturbation energy mainly associated to vortices and the boundary pressure work linked to these perturbations. For either a deceleration or an acceleration of the fluid, the first and second terms are positive. Thus, any velocity perturbation (positive or negative) leads to a creation of exergy which can be potentially transformed into useful work. Note that since mechanical exergy is fully recoverable, $\dot{\mathcal{X}}'_{m} = \dot{E}'_{m}$.

- $\dot{\mathcal{X}}'_{th} := \underbrace{\int_{S_o} \rho\delta e (\mathbf{V}' - \mathbf{s_e}') \cdot \mathbf{n}' \, \mathrm{d}S}_{\dot{E}'_{th}} + \underbrace{\int_{S_o} p_\infty (\mathbf{V}' - \mathbf{s_e}') \cdot \mathbf{n}' \, \mathrm{d}S}_{\dot{E}'_W} - \underbrace{T_\infty \int_{S_o} \rho\delta s (\mathbf{V}' - \mathbf{s_e}') \cdot \mathbf{n}' \, \mathrm{d}S}_{\dot{A}'}$ is the thermocompressible exergy wasted. The three terms composing it correspond respectively to the thermal energy outflow, the isobaric boundary pressure work and the total anergy outflow. This term highlights the fact that, contrary to mechanical exergy which can theoretically be fully recovered, only a part of the thermal energy available can be converted to useful work.

- $\dot{\mathcal{A}}'_{\phi} := \int_{\mathcal{V}} \frac{T_\infty}{T} \phi' \, \mathrm{d}\mathcal{V}$ corresponds to the anergy generation (i.e. the irreversible destruction of exergy) due to viscous phenomena appearing in the flow. It corresponds to a process converting mechanical energy into thermal energy in order to smooth the velocity field and is referred to as the viscous anergy, which is always positive.

- $\dot{\mathcal{A}}'_{\nabla T} := \int_{\mathcal{V}} \frac{T_\infty}{T^2} k (\nabla T)'^2 \, \mathrm{d}\mathcal{V}$ is the anergy generation due to the thermal mixing that uniformizes the temperature field while the system goes back to a thermal equilibrium state. Again, this term is always positive as it represents the destruction of exergy inside the control volume through an irreversible process.

- $\dot{\mathcal{A}}'_w := T_\infty \int_{S_w} [\![\frac{1}{T}\mathbf{q}' + \rho\delta s(\mathbf{V}' - \mathbf{s_e}')]\!] \cdot \mathbf{n}' \, \mathrm{d}S$ corresponds to the anergy generation due to the presence of discontinuous shockwaves in the flow.

- $\tau'_o := -\int_{S_o} (\overline{\overline{\tau}}' \cdot (\mathbf{V}' - \mathbf{V}'_\infty)) \cdot \mathbf{n}' \, \mathrm{d}S$. This term is the rate of work of the viscous force on the outer boundary linked to velocity perturbations.

- $\dot{\mathcal{X}}'_{qo} := -\int_{S_o} \left(1 - \frac{T_\infty}{T}\right) \mathbf{q}' \cdot \mathbf{n}' \, \mathrm{d}S$. This term corresponds to the thermal exergy outflow associated with heat conduction across the outer boundary of the control volume.

It is noted that $\dot{\mathcal{X}}'_r$ is an additional term that appears in the rotating frame of reference and does not correspond to the propulsive exergy defined by Arntz [15] projected in the rotating frame of reference.

IV. Numerical application: HAD-1 propeller case

A. Presentation of the case

The HAD-1 case geometry and a view of the surface mesh considered in this study are shown in Fig. 2. It corresponds to a 3-blade propeller in an external flow field with a spinner and a fixed cylinder extending downstream up to the limit of the computational domain. It was studied at ONERA within the European project MADELEINE [23] as a reference case for aerodynamics/aeroacoustics investigations. The blade geometry was designed and studied previously at ONERA [24] [25] to evaluate body-force models. A multiblock structured mesh composed of around 10.1 million points is used for the numerical computation. The blade surface mesh is composed of 129 points in the spanwise direction, and each radial section of the blade is discretized with 266 points in the chordwise direction (including 33 points for the blunt trailing edge). The y^+ value for the blade, spinner and downstream cylinder is in the order of 0.4 for the nominal operating regime. This corresponds to an "industrial" grid, in the sense that the grid topology and properties follow standard practice on aerodynamic performance prediction and are not specifically adjusted for the sake of the exergy analyses in this work. The force and torque convergence of CFD computations was pursued at least until a variation below 10^{-3} counts was observed over the last 1000 iterations. The boundary condition applied at all solid boundaries is a no-slip condition, i.e. the flow is viscous near the walls. Note that a free-slip wall boundary condition could have been considered without affecting the validity of the exergy balance of Eq. (13) or that of the following analysis.

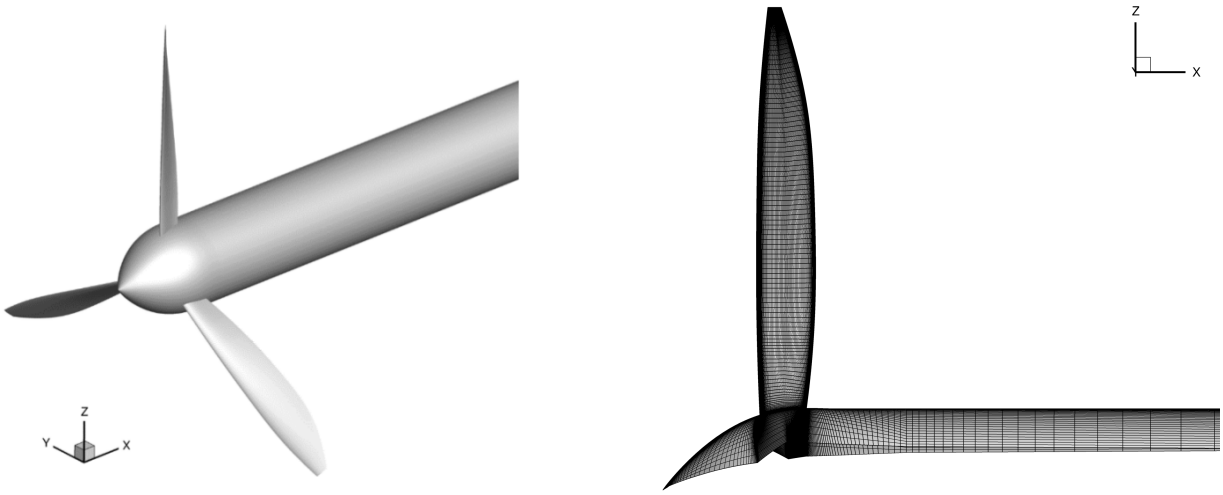

Fig. 2 HAD-1 propeller geometry (left) and side view of the mesh used (right).

The numerical computation that is post-processed with FFX is carried out with the ONERA-AIRBUS-SAFRAN CFD solver elsA [26], on a 120-degree azimuthal section with periodic boundary conditions. The CFD computations and the post-processing results were validated against a comparison with the complete 360° configuration. During the post-processing with FFX, several numerical operations are ensured in coupling with the Cassiopée open-source set of python modules for pre- and post-processing of CFD computations, developed at ONERA [27].

The steady Reynolds-Averaged Navier-Stokes (RANS) in the AVRF formulation supplemented by the one-equation Spalart-Allmaras turbulence model are solved in the numerical simulations. The propeller radius is $r_p = 0.8m$ and its angular velocity in the nominal operating regime is $\omega = 212.6$ rad.s^{-1}. The angle of attack and sideslip angle are considered null in this study. The freestream flow state (corresponding to the reference state used in exergy term computations in this case) in the HAD-1 nominal operating regime is defined with $\rho_\infty = 1.225$kg.m^{-3}, $T_\infty = 288.16$K and $M_\infty = 0.3$, with the corresponding Reynolds number $Re_\infty = 7.\ 10^6$. The computational domain extends in the x-direction between $x_{min} = -11.0m = -13.75r_p$ and $x_{max} = 18.9m = 23.625r_p$. The propeller is situated between the coordinates $x = -0.2m$ and $x = 0.2m$, with the fixed cylinder extending downstream up to the end of the computational domain. In the radial direction, the mesh extends up to $r_{max} \approx 13.8r_p$. Fig. 3 shows iso-surfaces of the Q-criterion colored with the relative Mach number.

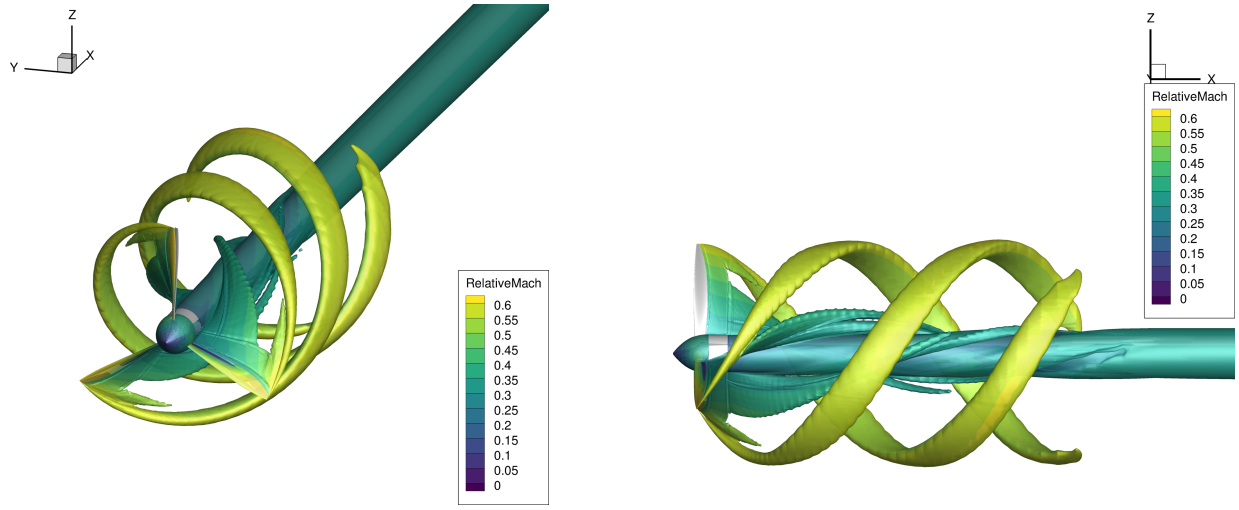

Fig. 3 HAD-1 iso-surface of the Q-criterion colored by the relative Mach number in perspective (left) and side (right) view. The computation and post-processing were performed in a 120° azimuthal section containing one blade.

B. Preliminary considerations

The walls in the HAD-1 case computation are all considered adiabatic for most applications (the sole exception being the investigation of an isothermal blade surface in Sec. IV.C.3), thus $\dot{\mathcal{X}}'_{qb} = 0$. As the case of application is one of external aerodynamics that does not involve a significant exchange of heat through its boundaries, and as their negligible values are confirmed numerically, the terms τ'_o and $\dot{\mathcal{X}}'_{qo}$ are also neglected in the following. Under these considerations, Eq. (13) becomes:

$$\dot{\mathcal{X}}'_r = W\dot{\Gamma}' + \dot{\mathcal{X}}'_m + \dot{\mathcal{X}}'_{th} + \dot{\mathcal{A}}'_\phi + \dot{\mathcal{A}}'_{\nabla T} + \dot{\mathcal{A}}'_w \tag{14}$$

The viscous and thermal anergy components are computed using the effective (viscous and turbulent) dissipation rate and the effective heat flux by conduction defined as:

$$\phi'_{eff} = (\overline{\overline{\tau}}'_{eff} \cdot \nabla') \cdot \mathbf{V}'$$
$$\mathbf{q}'_{eff} = -k_{eff}(\nabla T)'$$

where $\overline{\overline{\tau}}'_{eff} = (\mu_l + \mu_t)\overline{\overline{S}}'$ is the effective stress tensor and $k_{eff} = c_p\left(\frac{\mu_l}{Pr} + \frac{\mu_t}{Pr_t}\right)$ is the effective thermal conductivity. Additionally, the numerical computation of the wave anergy (for operating regimes in which a shockwave is formed) requires the isolation of a wave volume. This is done using a shockwave detection criterion based on the value of the relative Mach number projected in the pressure gradient direction (which is normal to the shockwave) [28, 29]. If the value of the normal relative Mach number is above a fixed threshold, the criterion is activated and indicates that a shockwave is formed. Several cell layers are then added around the detected wave volume to account for numerical

oscillations and cells within the boundary layer are excluded. Finally, a filter is applied (as was done by Lovely and Haimes [28] for unsteady analyses and Verley [29] in the frame of helicopter rotor performance investigations) to remove cells in which a shockwave is incorrectly detected in the far-field. This treatment is necessary, as small numerical errors in the gradient are amplified by the high values of the rotation velocity $\mathbf{s_e}'$ far from the propeller rotation axis, leading to inaccurate shock detection. The impact of the filter on the value of the wave anergy computed was investigated and found to be negligible for the HAD-1 case.

All terms of the exergy balance are normalized in the form of non-dimensional coefficients as (taking the viscous anergy $\dot{\mathcal{A}}'_\phi$ as an example):

$$C_{\dot{\mathcal{A}}'_\phi} = \frac{\dot{\mathcal{A}}'_\phi}{0.5\rho_\infty S_{ref} V'^3_\infty} \tag{15}$$

and their non-dimensional values are given in power counts (pc, 10^{-4}).

Two figures of merit are defined in order to characterize the propeller's efficiency in the exergy framework, and computed with FFX. The first one is:

$$\psi_p = \frac{W\dot{\Gamma}'}{\dot{\mathcal{X}}'_r} \tag{16}$$

which is referred to as the effective propulsive efficiency, i.e. the part of the exergy provided by the propeller that is actually used by the body to maintain its axial mechanical equilibrium (overall thrust, force equilibrium or drag). A second quantity is introduced:

$$\psi_{pr} = \frac{W\dot{\Gamma}' + \dot{\mathcal{X}}'_m + \dot{\mathcal{X}}'_{th}}{\dot{\mathcal{X}}'_r} \tag{17}$$

which is the reversible propulsive efficiency. This term should generally be higher than ψ_p and will always be below 1.0 in the case of Navier-Stokes simulations. This is because irreversibilities present in the flow lead to anergy generation and thus prevent the complete transformation of the exergy provided by the propeller into useful work. As such, the difference between an ideal efficiency of 1.0 and ψ_{pr} is attributed to irreversible losses of exergy (i.e. anergy generation), whereas the difference between ψ_{pr} and ψ_p is attributed to mechanical and thermal outflow of exergy from the control volume, which are theoretically recoverable. A modified design leading to a reduction of exergy outflows would thus lead to an increase of ψ_p (tending towards ψ_{pr}), considering that this could be done without modifying anergy generation. In practice however, a design modification would likely lead to a change of anergy generation within the control volume, and thus also to a different ψ_{pr} value than the original design. This would particularly be the case of a swirl-recovery device, the addition of which could lead to a reduction of exergy outflow but also inevitably to an increase in anergy generation. Swirl recovery can still lead to an overall benefit by an increase of effective efficiency, even though this would not reach the reversible efficiency of the isolated rotor blade. Therefore, such figures of merit provide a practical insight into the flow physics, as the difference between ψ_p and ψ_{pr} provides a quantification of reversible losses, whereas the difference between ψ_{pr} and 1.0 directly quantifies irreversible losses in the flow.

C. Numerical results

1. Evolution of exergy coefficients at different downstream stations for the nominal operating regime

In this section, the exergy balance is computed for a series of downstream limits of the control volume with the x-coordinate for each plane noted x_{TP} for the nominal operating regime (detailed in Sec. III). No shockwave is formed under these flight conditions, i.e. $\dot{\mathcal{A}}'_w = 0$. The values selected for x_{TP} start at $x_{TP_{min}} = -2.0m$ and are up to $x_{TP_{max}} = 5.0m$ in order to remain within regions of the flow with reasonable grid resolution. A step of $0.5m$ between each position is used. The station situated at $x_{TP} = 0m$ is excluded, as the downstream limit of the control volume intersects the propeller blades, making the physical interpretation of the exergy balance non-straightforward.

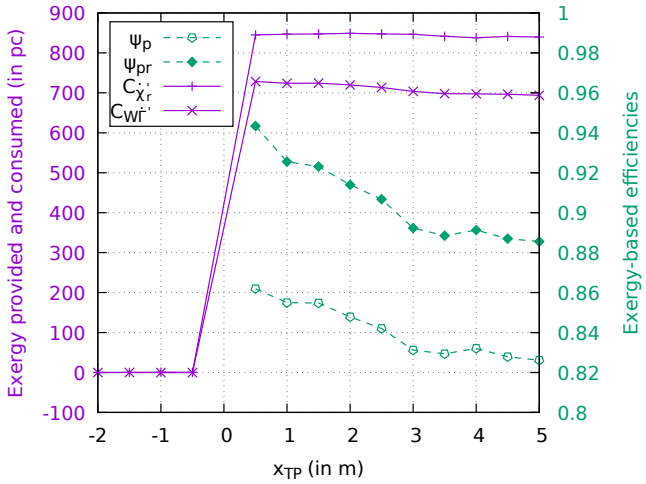

Fig. 4 Exergy provided and consumed by the system and efficiencies as functions of x_{TP}.

The values of the exergy provided by the propeller $\dot{\mathcal{X}}'_r$ and the exergy consumed to maintain a steady state $W\dot{\Gamma}'$, alongside its effective and reversible efficiencies are plotted in Fig. 4. It shows that $C_{\dot{\mathcal{X}}'_r}$ is equal to zero up to $x_{TP} = -0.5m$. This is because there is no exergy transferred from the propeller to the fluid up to the beginning of the spinner. It then reaches a value of approximately 845 pc, with a few variations which are due to the effect of the cylinder and some numerical noise. When the control volume includes the propeller blade, the curve for $C_{W\dot{\Gamma}'}$ follows the curve of $C_{\dot{\mathcal{X}}'_r}$ up to 729 pc before starting to drop. This shows that only part of the exergy supplied by the propeller is consumed by the system in order to produce thrust, the rest of it being wasted as exergy outflow or destroyed through anergy generation. It then decreases due to the presence of the cylinder downstream: indeed, viscous drag increases when a larger part of the cylinder is included in the control volume, which in turn leads to a lower overall force in the axial direction.

The values for ψ_p and ψ_{pr} are plotted for $x_{TP} \geq 0.5m$: the efficiency of the propeller has a clear interpretation only when the propeller is included in the control volume. In Fig. 4, as a longer section of the cylinder is included in the control volume, the reversible and effective efficiencies decrease. This is consistent with the evolutions of $C_{\dot{\mathcal{X}}'_r}$ and

$C_{W\dot{\Gamma}'}$ which show that the performance is degraded when x_{TP} increases. But the exergy balance gives an indication of the room for improvement towards the reversible propulsive efficiency by attempting to recover the components of exergy outflow. For $x_{TP} = 2.0m$, this efficiency could be increased from 84.8% up to a maximal efficiency of 91.4% by reducing the exergy outflow from the control volume to zero without additional anergy generation (which is not feasible in practice, cf. Sec. IV.B). A slope reduction is observed for both efficiency curves beyond $x_{TP} = 3.0m$ because the cell size increases and the mesh becomes coarser, leading to higher numerical imprecision.

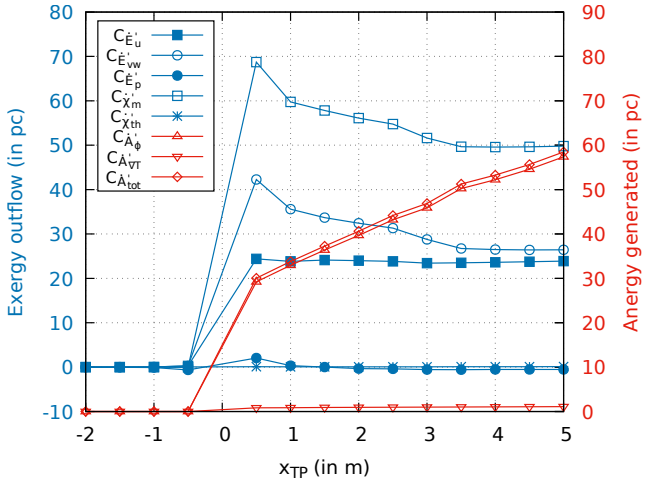

Fig. 5 Components of exergy outflow and anergy generated as function of x_{TP}

The exergy outflow, i.e.wasted, and the anergy generated are then plotted in Fig. 5. All components are confirmed to be null before the propeller is included inside the control volume. Then, large variations can be observed when the transverse plane is moved from upstream to downstream of the propeller. In the vicinity of the propeller, the fluid particles are accelerated, leading to an increase in $C_{\dot{E}'_u}$, $C_{\dot{E}'_{vw}}$ and $C_{\dot{E}'_p}$, the sum of these three terms giving an increase in mechanical exergy outflow. Pushing the transverse plane further downstream leads to a decrease of all exergy outflow components: exergy is destroyed by irreversible effects which correspond to an increase in anergy generation. The main irreversible effect appearing here is the dissipation of the flow exergy by viscous effects, as $C_{\dot{\mathcal{A}}'_\phi}$ is much higher than $C_{\dot{\mathcal{A}}'_{\nabla T}}$. This and the very low values for the thermal exergy $C_{\dot{\mathcal{X}}'_{th}}$ highlight that temperature variations and thermal exchanges are secondary compared to viscous effects and mechanical exergy outflow for this configuration at this reference state. The values for the coefficients of the exergy balance with four different planes limiting the control volume are shown in Table 1, with the residual coming from the imbalance between the two sides of the exergy balance equation (computed as Residual = LHS-RHS). The Exergy-Waste Coefficient (EWC), introduced by Arntz [15] is also computed using the quantities expressed in the relative frame as:

$$EWC = \frac{\dot{\mathcal{X}}'_m + \dot{\mathcal{X}}'_{th}}{\dot{\mathcal{X}}'_m + \dot{\mathcal{X}}'_{th} + \dot{\mathcal{A}}'_{tot}} \tag{18}$$

and corresponds to the part of unused exergy that is theoretically recoverable at each corresponding x_{TP} position.

x_{TP} (m)	$\frac{x_{TP}}{r_p}$	$C_{\dot{\mathcal{X}}'_r}$	$C_{W\dot{\Gamma}'}$	$C_{\dot{E}'_u}$	$C_{\dot{E}'_{vw}}$	$C_{\dot{E}'_p}$	$C_{\dot{\mathcal{X}}'_m}$	$C_{\dot{\mathcal{X}}'_{th}}$	$C_{\dot{\mathcal{A}}'_\phi}$	$C_{\dot{\mathcal{A}}'_{\nabla T}}$	Residual	EWC
0.2	0.25	846.67	733.47	23.37	49.25	3.03	75.65	0.41	26.72	0.81	9.60	0.73
0.5	0.625	845.21	728.51	24.39	42.29	2.05	68.73	0.09	29.22	0.83	17.83	0.70
1.0	1.25	846.78	723.94	23.83	35.58	0.33	59.75	0.06	32.95	0.87	29.21	0.64
2.0	2.5	849.06	719.85	24.00	32.43	-0.34	56.09	0.07	39.68	0.93	32.44	0.58

Table 1 Exergy balance computed for different downstream transverse plane positions. All exergy coefficients except the EWC are expressed in power counts.

When the transverse plane is placed further downstream, the residual of the exergy balance increases. This is due to numerical effects, a subject which is further investigated and discussed in Appendix A. Table 1 also shows that the more downstream the transverse plane, the less exergy flows out of the control volume relative to the total anergy generated, which appears as a decrease of the EWC. This progressive dissipation is also highlighted by the histogram representing the different exergy coefficients contributions in Fig. 6. The numerical precision aspects are further discussed in Appendix A.2.

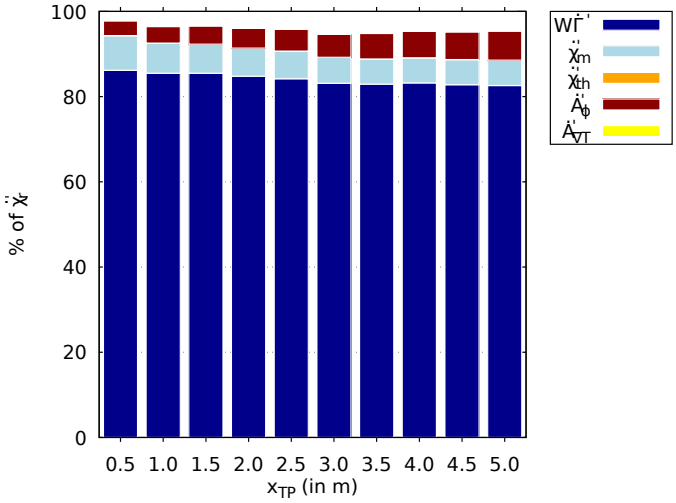

Fig. 6 Contributions of the different exergy coefficients as percentages of $\dot{\mathcal{X}}'_r$.

2. Physical analysis of the nominal operating regime using exergy and anergy field visualisations

Visualisations of the exergy balance terms allow one to describe the physical phenomena taking place in the control volume. Several stations at fixed x coordinate are used to view where the different terms of the exergy balance have significant values and to what phenomena they can be related. Three stations are selected at the coordinates $x = 0.2m$,

$x = 0.5m$ and $x = 1.0m$, as represented in Fig. 7.

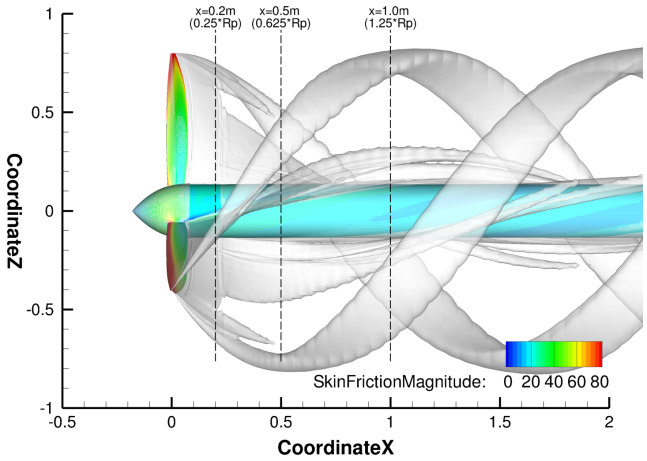

Fig. 7 Side view of the downstream stations at $x = 0.2m$, $x = 0.5m$ and $x = 1.0m$ selected for flow field visualisation. A skin friction magnitude contour and an iso-surface of the Q-criterion are also shown.

The contours of exergy outflow and viscous anergy generation are then plotted for these stations in Fig. 8. The propeller geometry is superposed to visualise the blade geometries and positions.

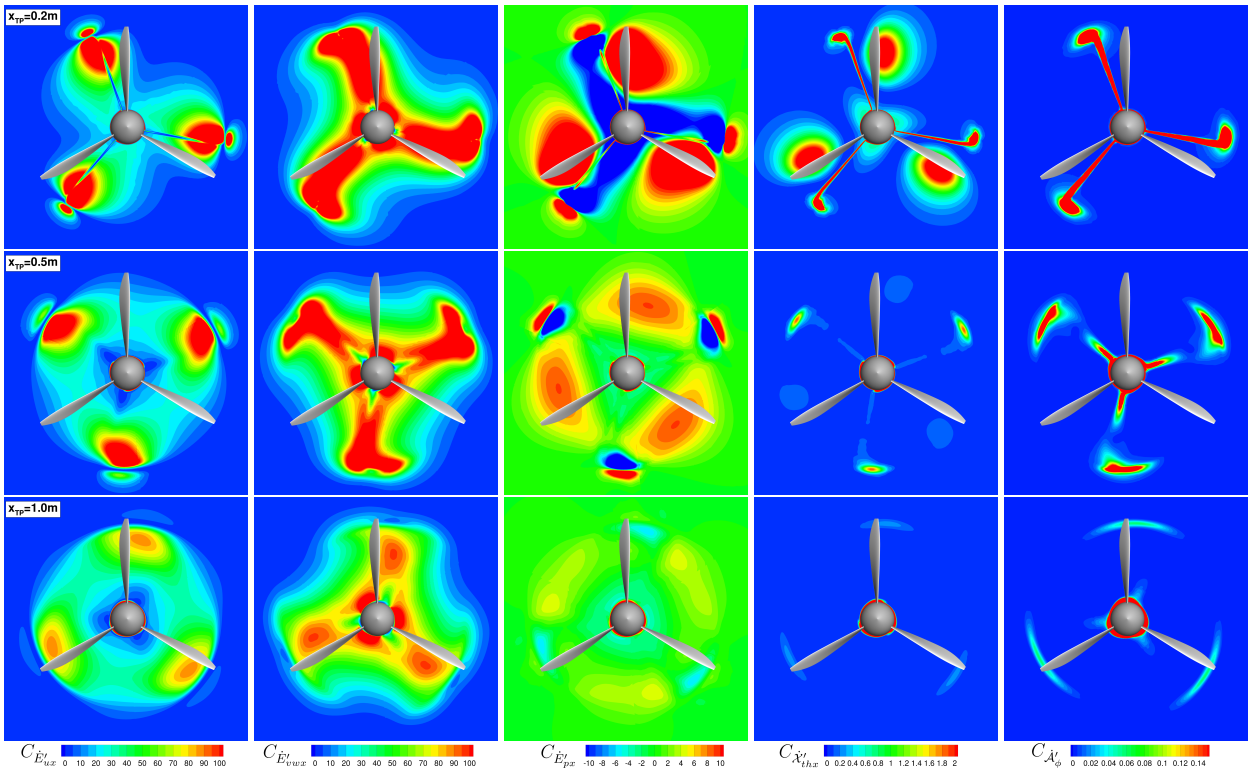

Fig. 8 Contours of exergy balance components at $x_{TP} = 0.2m$ (first row), $x_{TP} = 0.5m$ (second row) and $x_{TP} = 1.0m$ (third row). The streamwise kinetic perturbation energy, transversal kinetic perturbation energy, boundary pressure rate of work, thermocompressible exergy outflow and viscous anergy generation are respectively represented in columns one to five.

A system of three vortices attached to the propeller wake is observed downstream of the propeller. Inside these structures, the pressure and velocity are different from their values in the reference state leading to exergy components that are non-null. The first and second columns of Fig. 8 show that the flow velocity is perturbated by the propeller, leading to a large region with streamwise and transversal perturbation kinetic exergy outflow, which also appears for the transversal perturbation kinetic energy. The system of vortices is also clearly visible in the first column of Fig. 8 with a local axial perturbation kinetic energy outflow at the tip of the blade wake. These structures can also be distinguished from the boundary layer of the cylinder, with a distinct kinetic energy variation in the region close to it. These observations are confirmed with the pressure-work rate contours related to these velocity perturbations plotted in the third column of Fig. 8. Indeed, tip vortices can be clearly distinguished from the blade wake, characterised by a decrease of static pressure. For this last term, in addition to these structures, a large zone with higher pressure that does not appear to be rotating with the wake of the blades is observed. This also appears with thermocompressible exergy contours in the fourth column of Fig. 8, where the rotating wake of the blades can clearly be followed as there is thermal exergy available in this wake and at the center of the tip vortices. The non-rotating zone identified previously is also present in the case of the thermal exergy outflow (fourth column). This zone actually corresponds to the potential effect of the high pressure region due to the flow passing close to the blades of the propeller. This means that this zone is actually rotating at the same velocity as the propeller, making it appear motionless in the rotating frame.

These figures allow to describe the physics of the flow by looking at the components of exergy outflow. The kinetic energy present inside the vortices and the propeller wake is then progressively dissipated primarily by the viscous forces, as indicated by the increase of viscous anergy generation discussed above (see Fig. 5). The same observation can be made in terms of thermal exergy, which is dissipated primarily through thermal mixing corresponding to an increase of thermal anergy. This appears for example on viscous anergy contours (fifth column of Fig. 8). As stated previously, the exergy available in the blades' wake and in the tip vortices is dissipated, leading to regions of anergy production that follow the regions of exergy outflow discussed above. Note that it was also confirmed numerically that the thermal anergy generation contours are overall similar to viscous anergy contours, at a lower magnitude. The magnitude of the generated anergy in sections positioned further downstream is lower due to viscous effects and thermal mixing causing velocity and thermal gradients to be of lower magnitude as well. The regions of high pressure and thermal exergy attached to the blades do not appear in anergy contours as they are not linked to viscous and thermal dissipation. Part of the dissipation also occurs in the boundary layer of the cylinder extending up to the end of the control volume, as Fig. 5 also shows.

3. Specific case of heated blades under nominal flight conditions

The thermal effects present inside the control volume are also considered in the exergy balance for the nominal operating regime. Hence, the particular case of a propeller with heated blades is studied in this section to analyze

the effect this additional condition has on the flow exergy balance. This is done by imposing an isothermal boundary condition on the blade (i.e. not the spinner and downstream cylinder) with two different wall-temperature values T_b of respectively 300K and 350K. The term $\dot{\mathcal{X}}'_{qb}$ is then not null anymore and must be computed in the exergy balance. The figures of merit for the efficiency of the propeller are also redefined to account for the additional exergy provided by the configuration studied, due to the non-adiabatic wall boundary conditions:

$$\psi_p = \frac{W\dot{\Gamma}'}{\dot{\mathcal{X}}'_r + \dot{\mathcal{X}}'_{qb}} \qquad \psi_{pr} = \frac{W\dot{\Gamma}' + \dot{\mathcal{X}}'_m + \dot{\mathcal{X}}'_{th}}{\dot{\mathcal{X}}'_r + \dot{\mathcal{X}}'_{qb}} \tag{19}$$

The evolution for the different exergy coefficients in the case of heated blades is then plotted for different stations locations for each isothermal case in Figs. 9 and 10.

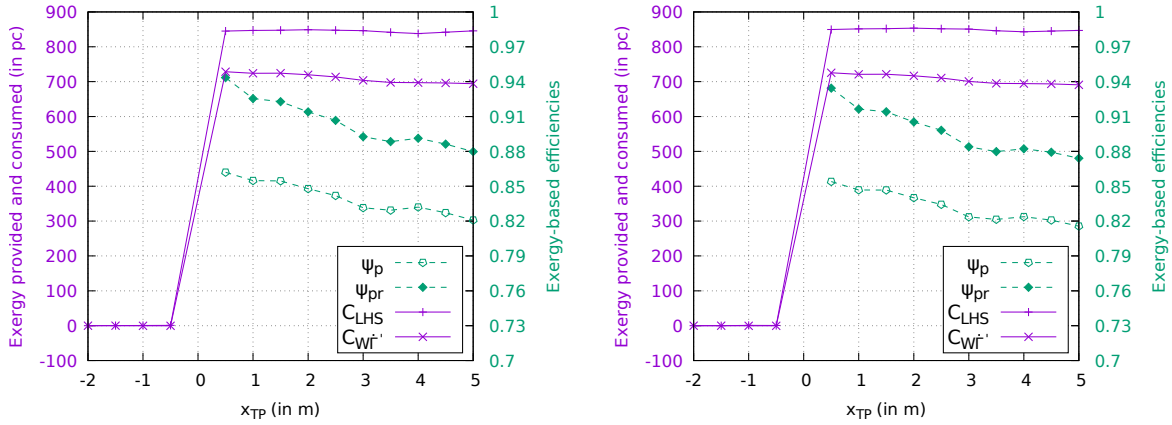

Fig. 9 Exergy-based shaft power, consumed power and efficiencies as functions of x_{TP} for $T_b = 300K$ (left) and $T_b = 350K$ (right).

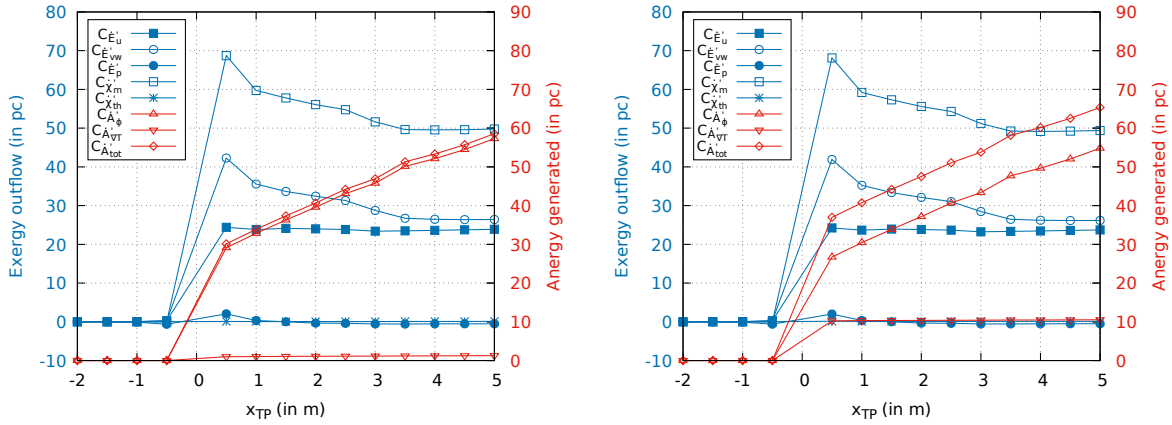

Fig. 10 Components of exergy outflow and anergy generated as functions of x_{TP} for $T_b = 300K$ (left) and $T_b = 350K$ (right).

Heating the blade has an effect on both the efficiency of the propeller and the exergy and anergy coefficients of the balance. Fig. 9 shows that increasing T_b leads to an increase of the total exergy supplied to the fluid. As this additional exergy supplied by thermal conduction is not converted into useful work, a lower efficiency is obtained for higher blade temperatures. Following the effective efficiency behavior ψ_p, ψ_{pr} decreases when T_b increases. Fig. 10 shows that this is because almost all the thermal exergy provided by the higher-temperature wall surface is dissipated through thermal mixing, i.e. thermal anergy generation. There is a steep increase of thermal anergy which becomes non-negligible for higher values of T_b, while levels of thermal exergy outflow stay very low in the wake of the blade. The thermal anergy remains almost constant when pushing the transverse plane further, demonstrating that most of the thermal diffusion takes place in the vicinity of the propeller blade. The other coefficients of the exergy balance are less impacted when modifying T_b. Overall, this means that taking into account a higher temperature of propeller blade surfaces does not lead to a significant increase in the exergy outflow decomposition: the coefficients linked to mechanical effects are not significantly affected, while the thermal exergy outflow remains at low values. It should however be noted that the modifications are small but quantifiable. Fig. 10 also shows that the viscous anergy decreases slightly when increasing the wall temperature T_b.

Table 2 shows the exergy balance coefficients values obtained for $x_{TP} = 0.2m$ with the adiabatic case, the case where $T_b = 300K$ and the case with the highest wall temperature $T_b = 350K$. As T_b is increased, lower values are obtained on the terms of the exergy balance linked to mechanical effects ($\dot{\mathcal{X}}'_r$,$W\dot{\Gamma}'$,$\dot{\mathcal{X}}'_m$ and $\dot{\mathcal{A}}'_\phi$) even though the angular velocity is constant. This could be linked to the thickening of the thermal boundary layer leading to a displacement of the viscous boundary layer farther from the walls.

Case	$C_{\dot{\mathcal{X}}'_{qb}}$	$C_{\dot{\mathcal{X}}'_r}$	$C_{W\dot{\Gamma}'}$	$C_{\dot{E}'_u}$	$C_{\dot{E}'_{vw}}$	$C_{\dot{E}'_p}$	$C_{\dot{\mathcal{X}}'_m}$	$C_{\dot{\mathcal{X}}'_{th}}$	$C_{\dot{\mathcal{A}}'_\phi}$	$C_{\dot{\mathcal{A}}'_{\nabla T}}$	Residual	EWC
Adiabatic	0	846.67	733.47	23.37	49.25	3.03	75.65	0.41	26.72	0.81	9.60	0.73
$T_b = 300K$	0.08	846.67	733.42	23.37	49.23	3.03	75.64	0.42	26.63	0.96	9.48	0.73
$T_b = 350K$	8.49	842.50	730.52	23.25	48.80	2.98	75.03	0.72	24.22	10.23	10.27	0.69

Table 2 Exergy balance computed for adiabatic and heated blade cases at $x_{TP} = 0.2m$. All exergy coefficients except the EWC are expressed in power counts.

4. Study of the propeller under different freestream flow conditions

The exergy analysis is now performed for the adiabatic wall case under different freestream flow conditions to evaluate the performance of the propeller in off-design operating points. This study is performed at a fixed pitch angle and the control volume is limited at $x_{TP} = 0.2m$ in order to focus on the rotating parts of the body, i.e. the spinner and

the blades. The freestream velocity V_∞ is then modified in order to adjust the propeller advance ratio J, defined as:

$$J = \frac{V_\infty}{2r_p N} \tag{20}$$

where $N = \frac{\omega}{2\pi}$ is the angular velocity expressed in rotations per second.

Three different angular velocity values are then selected, corresponding to $\omega = 212.6$ rad.s^{-1}, $\omega_{90\%} = 191$ rad.s^{-1} and $\omega_{110\%} = 234.4$ rad.s^{-1}, i.e. the nominal angular velocity to which roughly 10% of its value is added or substracted. For each angular velocity, numerical computations are performed at a M_∞ values varying between 0.24 and 0.50, with a step of 0.02. The rest of the freestream values are kept constant, meaning that this variation corresponds to a variation of V_∞.

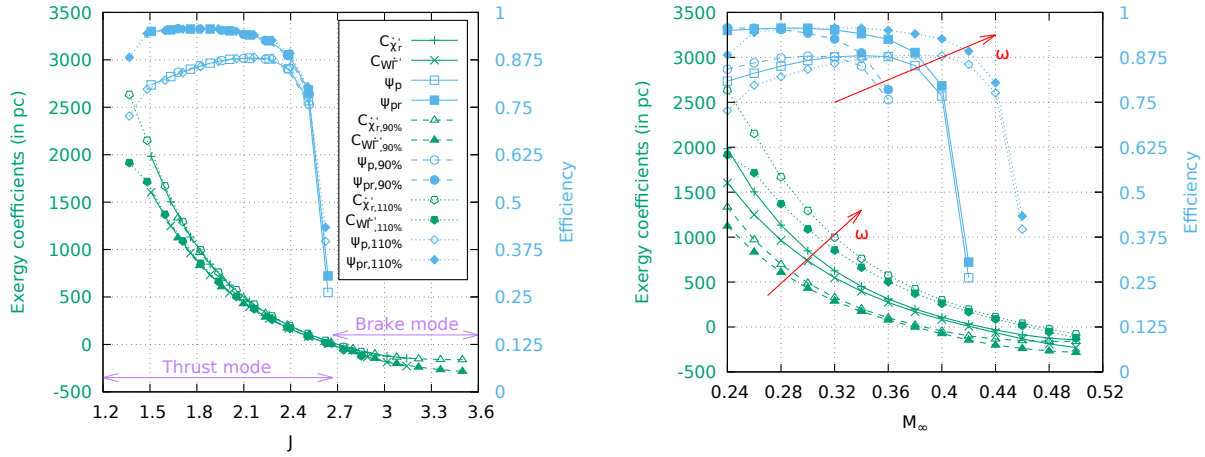

Fig. 11 Exergy-based shaft power, consumed power and efficiencies as functions of the propeller advance ratio J (left) and of M_∞ (right) for $x_{TP} = 0.2m$ with ω (solid lines), $\omega_{90\%}$ (dashed lines) and $\omega_{110\%}$ (dotted lines).

The exergy-based efficiencies, the corresponding net power consumed and the exergy provided by the propeller are then computed and plotted in Fig. 11. For all three angular velocities, the more J increases, the less shaft power is transferred to the fluid and the less mechanical power associated to the streamwise net axial force is consumed. The evolution of ψ_p shows that, for an angular velocity of 212.6 rad.s^{-1}, the maximum effective efficiency is obtained at a freestream state with $M_\infty = 0.36$ (corresponding to $J = 2.26$). Further increasing the freestream Mach number leads to a steep decrease in the propeller efficiency, with no torque converted to thrust (i.e. $W\dot{\Gamma}' = 0$) and no shaft power transferred to the fluid ($\dot{\mathcal{X}}'_r = 0$) obtained for a J value between 2.6 and 2.8. For higher J values, the propeller is no longer producing an overall propulsive force, but instead generates more drag than thrust (i.e. $W\dot{\Gamma}' < 0$). Similarly, the propeller is not providing power to the fluid for higher J values but rather absorbing power ($\dot{\mathcal{X}}'_r < 0$). Modifying the angular velocity and plotting these curves for the same range of M_∞ values allows to translate the global shape of the curve on the right graph of Fig. 11: indeed, the M_∞ value corresponding to the optimal effective efficiency is lower when ω decreases, while it is higher when ω increases. The left graph of Fig. 11 shows that modifying the angular

velocity does not change the trend, nor the values of the different quantities plotted, as the curves overlap. This is expected for standard performance parameters (i.e. thrust, torque and effective propulsive efficiency), and also appears for the reversible propulsive efficiency. Thus, whereas changing the angular velocity indeed leads to a change of the optimal freestream velocity in terms of effective and reversible efficiency, this corresponds to the same optimal value of the advance ratio.

Plotting ψ_{pr} gives an estimation of the reversible efficiency that could be theoretically obtained for each different operating regime. Its behavior is not the same below the optimal J and M_∞ than when going above. For example, for ω = 212.6 rad.s^{-1}, while the reversible efficiency that could be theoretically obtained remains almost constant at a value close to 95% for M_∞ values below 0.32, it then starts decreasing and approaches the effective efficiency curve at M_∞ = 0.36, which it follows very closely in the efficiency drop part, as M_∞ keeps increasing. The curve for the reversible efficiency is also shifted towards higher values of M_∞ when increasing the angular velocity, delaying its sudden decrease towards higher M_∞ values, whereas performance degradation is also observed at low M_∞ values for the highest angular velocity studied. Plotting ψ_{pr} as a function of J again leads to an overlap of the curves for the three different angular velocities investigated. The same trend of a decrease of the reversible efficiency is also observed for J values above 2, with values of ψ_p and ψ_{pr} being closer for J = 2.26, beyond which both quantities decrease significantly. This means that working at operating regimes with J values below the optimal one leads to a decreased effective efficiency due partly to high amounts of wasted exergy, while working above it leads to a steep decrease in efficiency that is mostly due to irreversible destruction of exergy (cf. Section IV.B).

A more detailed physical insight is obtained from the evolution of the components of the exergy balance for these different operating regimes at a fixed ω = 212.6 rad.s^{-1} value, shown in Fig. 12. The contribution of the different coefficients is also plotted in Fig. 12 as a proportion of $\dot{\mathcal{X}}'_r$, i.e. the exergy provided by the propeller, for J values where $\dot{\mathcal{X}}'_r$ is positive. Figs. 11 and 12 correspond to a characteristic performance curve of the propeller with respect to J in terms of the exergy balance.

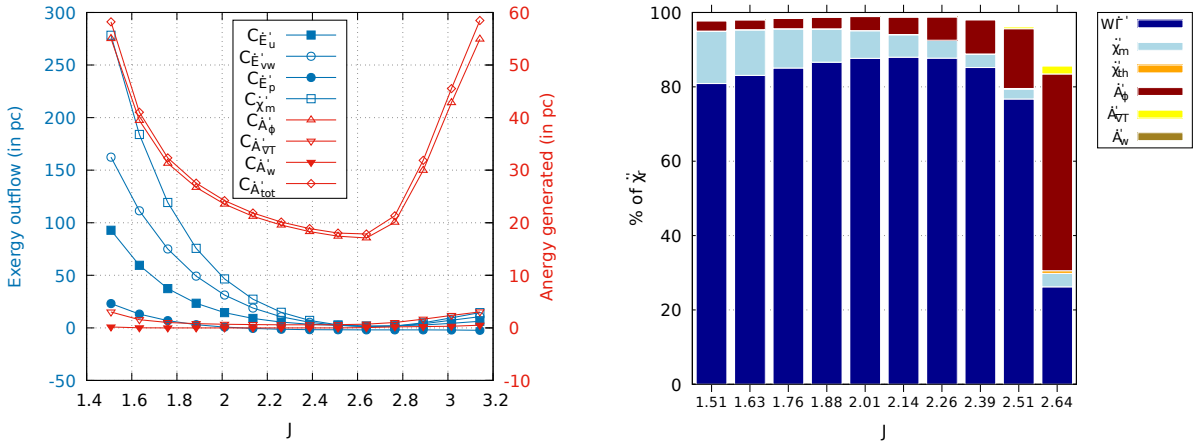

Fig. 12 Exergy outflow and anergy generated as functions of the advance ratio for $\omega = 212.6$ rad.s^{-1} and $x_{TP} = 0.2m$.

Fig. 12 shows that there is a steep decrease both in mechanical exergy outflow and in anergy generation when approaching the optimal operating regime in terms of efficiency. However, the mechanical exergy outflow decreases much faster than the anergy generation, with a decrease between the minimum value of J and the optimal one in the order of 300 power counts, while the anergy generation decreases by roughly 35 power counts. It can also be deduced that the optimal operating regime, situated at $J = 2.26$ for this angular velocity, does not correspond to a minimum of exergy destruction (i.e. anergy generation) but rather to a low anergy generation combined with low levels of mechanical exergy outflow. These observations are clearly visible on the histogram plotted in Fig. 12, in which the part of exergy dissipated through viscous anergy generation remains low. Exergy outflow on the other hand is drastically reduced when approaching the optimal operating regime, as more exergy provided is converted into useful work. This highlights the importance of using a complete exergy balance formulation to investigate the propeller's performance, instead of an individual component. Furthermore, when the efficiency starts decreasing significantly ($J \geq 2.39$), the anergy generation decreases slightly while the mechanical exergy outflow remains close to zero. For these values of J, Fig. 12 shows more clearly that the part of exergy outflow from the control volume varies much less than that dissipated through the generation of viscous anergy. This means that rather than converting more exergy outflow into useful work, a more significant part of it is destroyed through irreversible processes. At higher J values the exergy outflow remains low, and the absolute total anergy generation increases with a steeper slope than the one corresponding to the decrease observed at low and medium J values. This explains why the reversible efficiency drops alongside with the effective efficiency (cf. Fig. 12). In the range of J values corresponding to a braking mode (less thrust than drag), the exergy outflow remains very low while the total anergy (mainly viscous anergy) increases significantly. Finally, the wave anergy evolution is also plotted as it is not zero for all operating regimes explored. A shock is formed on the outer part of the blades when J is either sufficiently high or low, due to the increase of Mach number based on the relative velocity. A precision study for the different operating regimes investigated above is presented in Appendix A.3.

The Exergy Waste Coefficient (Eq. (18)) is plotted in Fig. 13 at different positions of the transverse plane downstream of the propeller for several values of the advance ratio. It shows that the EWC decreases downstream of the propeller as the exergy is dissipated, mostly through viscous anergy generation in the boundary layer of the cylinder and in the wake of the blades. Increasing the advance ratio from its minimum value towards the optimal J value of 2.26 leads to a lower EWC in the propeller wake region, corresponding to a decrease in the relative exergy wasted and a decrease of the absolute anergy generated (cf. Fig. 12). Further increasing the advance ratio leads to EWC levels that remain low for all transverse plane positions, as the level of exergy outflow is very low and the anergy generated is significant. As the propeller switches to a brake mode ($J \geq 2.76$), levels of EWC do not get closer to zero but rather increase again slightly. The switch from thrust mode to brake mode is thus not clearly depicted through the EWC. This coefficient rather underlines the decomposition of the part of the exergy provided by the rotating shaft and not used for producing thrust into a recoverable (i.e. exergy outflow) and a non-recoverable (i.e. anergy generation) part at each transverse plane position. While switching to a brake mode leads to higher levels of anergy generated (as shown in Fig. 12), it also leads to higher levels of exergy wasted in the wake of the propeller. The change of operating regime appears more clearly on coefficients related to the exergy provided by the rotating shaft and consumed to produce thrust, i.e. $\dot{\mathcal{X}}'_r$ and $W\dot{\Gamma}'$.

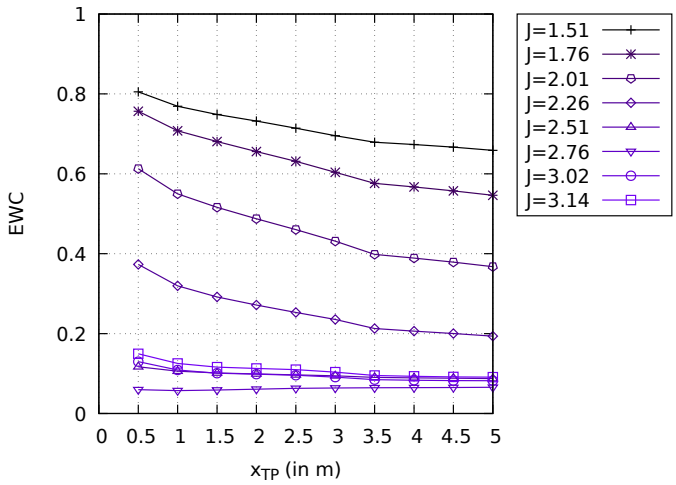

Fig. 13 Variation of the EWC as function of x_{TP} at different J values for ω = 212.6 rad.s^{-1}.

The physical explanation for these exergy terms and efficiency evolutions is given using a schematic illustration of the velocity triangle for one blade airfoil section shown in Fig. 14. It shows that increasing the reference velocity magnitude V_∞ or decreasing the angular velocity ω leads to a lower local relative angle of attack α_r for the different blade sections. Hence, when V_∞ increases sufficiently, corresponding to an increase of the propeller advance ratio J, the relative angle of attack becomes negative and the propeller starts to slow down the system under study rather than providing a propulsive force. On the contrary, decreasing V_∞ or increasing ω leads to an increase in this local angle of attack, which means that for low enough J values a stall phenomenon is observed on different blade sections, which

also decreases the efficiency obtained. This phenomenon appears for the angular velocity $\omega_{110\%}$ at the lowest J value investigated, where ψ_{pr} starts decreasing alongside ψ_p (see Fig. 11).

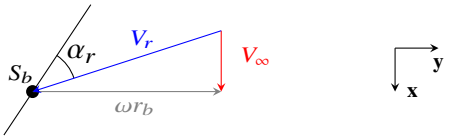

Fig. 14 Velocity triangle for a blade section at a radius r_b. Only the airfoil's chord line is represented.

This evolution of the angle of attack can also be observed in pressure contours at a fixed radius of $R = 0.75$m, as shown in Fig. 15. Streamtraces based on the relative velocity components also highlight the presence of a recirculation bubble appearing when the propeller switches to a brake mode, i.e. for higher values of M_∞.

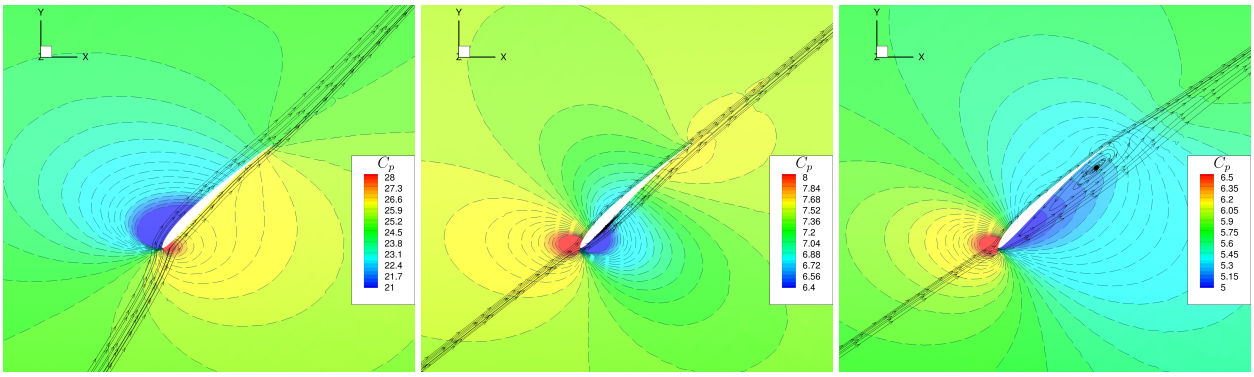

Fig. 15 Pressure coefficient contours and streamlines based on relative velocity around one blade section situated at a fixed radius of R = 0.75m for $J = 1.51$ (left), $J = 2.76$ (middle) and $J = 3.14$ (right), at ω = 212.6 rad.s^{-1}.

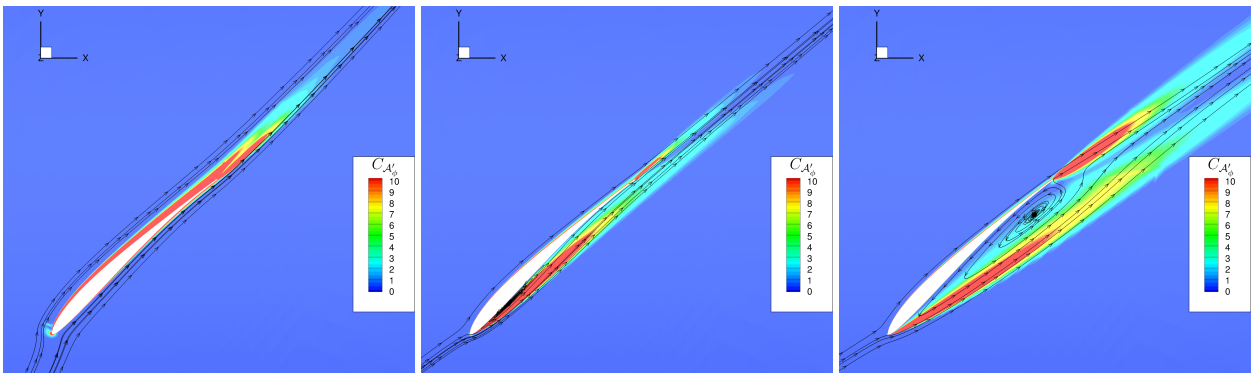

Fig. 16 Viscous anergy contours for $J = 1.51$ (left), $J = 2.76$ (middle) and $J = 3.14$ (right), for $\omega = 212.6$ rad.s^{-1} at a fixed radius R = 0.75m.

In addition to these pressure contours, contours of local viscous anergy generation are also plotted for this blade section in Fig. 16. When the local relative angle of attack is positive, the viscous anergy generation is mostly located on the upper surface and in the wake of the airfoil section. When it becomes negative, corresponding to a higher freestream

Mach number and advance ratio, viscous dissipation mainly occurs near the lower surface and in the wake of the blade section, with a notable region of anergy generation close to the trailing edge. The presence of a recirculation bubble is also identified, with a region of low anergy generation situated close to the airfoil lower surface and one of high anergy generation notable in the border of the bubble, where velocity gradients are of significant magnitude.

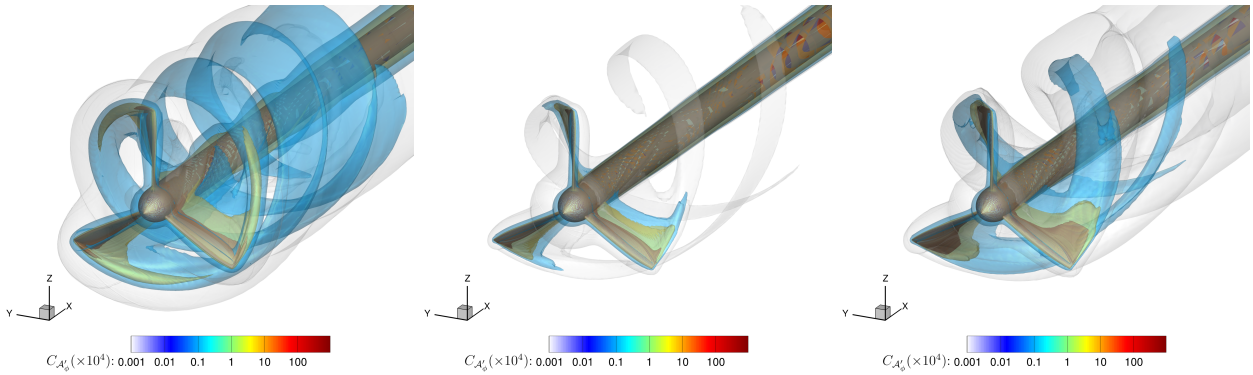

Fig. 17 Iso-surfaces of viscous anergy for J = 1.51 (left), J = 2.76 (middle) and J = 3.14 (right) for ω = 212.6 rad.s^{-1} in perspective view.

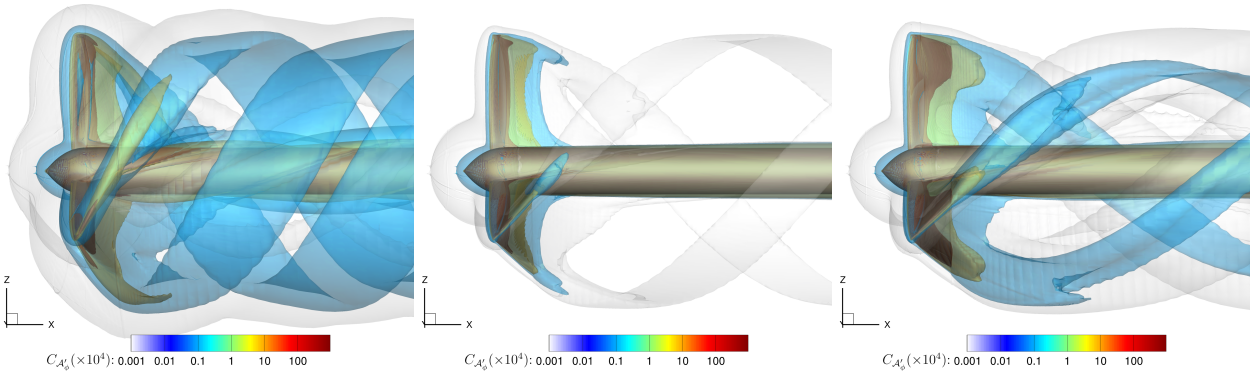

Fig. 18 Iso-surfaces of viscous anergy for J = 1.51 (left), J = 2.76 (middle) and J = 3.14 (right) for ω = 212.6 rad.s^{-1} in side view.

Finally, iso-surfaces of viscous anergy for these three cases are shown in Figs. 17 and 18. These are consistent with the analyses presented in Fig. 12. The case with M_∞ = 0.44 (J = 2.76) is linked to lower levels of anergy generation in the wake of the blades, with viscous anergy being primarily generated closer to the propeller surface. For the two other freestream Mach numbers, the anergy generated remains significant in the blade tip vortices and the wake of the blade, explaining the high levels of anergy generation shown in Fig. 12. While both the J = 1.51 and the J = 3.14 cases correspond to high levels of anergy generation, the iso-surfaces indicate that the physics involved are different. At the lower J value, viscous anergy is mainly generated close to the blade and in its wake, with corresponding iso-surfaces following the vortices. The mechanical exergy outflow inside the vortex structure is progressively dissipated, corresponding to high levels of anergy generation. At the higher J = 3.14 value, although non-negligible levels of

anergy generation are also observed inside the wake vortices, its main part is situated close to the propeller. More specifically, a structure of notable anergy generation is observed close to the propeller blade tip. As for the case at $J = 2.76$, the dissipation is mostly located close to the propeller with almost no viscous anergy generated in the wake of the blades. This analysis is in agreement with the EWC evolution in the propeller's wake when changing the value of J. The levels of exergy outflow are higher when the local relative angle of attack is further from zero due to the physical phenomena inducing significant flow perturbations appearing at those operating regimes. Consequently, the exergy outflow is close to being null close to the propeller for $\alpha_r \approx 0$ and consequently the EWC reaches its minimum value, even though the dissipation is lower than for higher J values (corresponding to lower negative values of α_r). The EWC then increases again with J, but does not reach the levels attained for the lowest advance ratio values as the dissipation remains predominant with respect to the levels of exergy outflow obtained.

Radial distributions of anergy production are then plotted in Fig. 19 for several operating regimes, in order to identify the main regions of anergy production. These are computed in a control volume limited in the x-direction by $-0.2m \leq x \leq 0.2m$ and in the radial direction by $0.0m \leq r \leq 1.2r_p$. As a consequence, the contribution of the fixed cylinder is excluded and the full blade geometry is included therein. The control volume is then regularly divided in the radial direction into 80 domains, and the anergy generated corresponding to each domain is computed and plotted as a point in Fig. 19. The $\dot{\mathcal{A}}'_\phi$ and $\dot{\mathcal{A}}'_{\nabla T}$ distributions show two main areas of irreversible dissipation for all the operating regimes, situated at the root and near the tip of the blade. The highest viscous dissipation at the root and the tip of the blade are respectively obtained for $J = 1.51$ and $J = 3.14$. For $J = 1.51$, skin friction magnitude contours (shown in Fig. 20) indicate that the anergy generation is linked to flow separation on the suction side of the propeller sections, particularly visible at the root of the blade. For $J = 3.14$, flow separation occurs at the root and in a large region near the tip of the blade. This explains the significant anergy generation observed at this radius range, and is linked to the flow structures appearing and discussed on the iso-surfaces of viscous anergy in Figs. 17-18. The $\dot{\mathcal{A}}'_w$ radial distribution shows that shocks are formed at a different radius and with different intensities for low and high values of J, the strongest shock being detected at $J = 3.14$. For this value of the advance ratio, the wave anergy locally reaches negative values close to zero. This is due to numerical oscillations close to the shock which can lead to local negative values of the wave anergy. The shock contribution is only properly accounted for when the integration is performed on a wave volume enclosing all those oscillations. As a consequence, the wave anergy computed for the complete shockwave must always be positive, but it is possible for it to be locally negative.

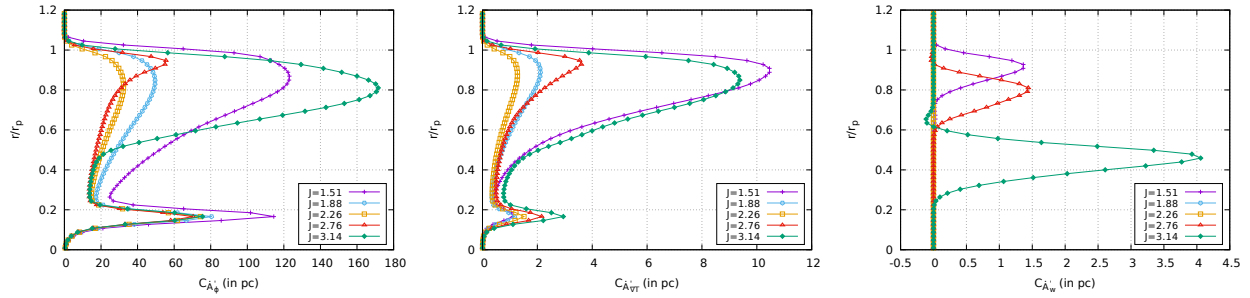

Fig. 19 Radial distribution of anergy production for different operating regimes. The control volume is limited in the x-direction with $-0.2m \leq x \leq 0.2m$.

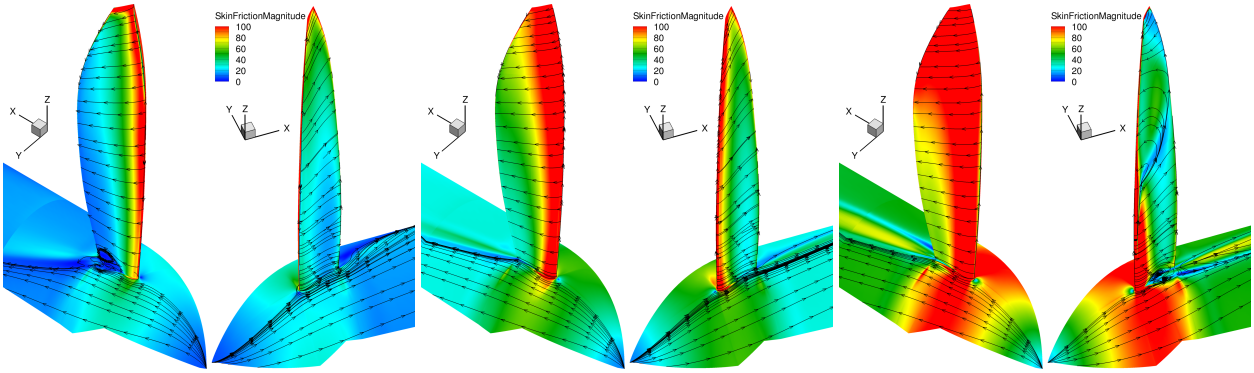

Fig. 20 Skin friction magnitude contours with streamtraces based on the skin friction components for $J = 1.51$ (left), $J = 2.26$ (middle) and $J = 3.14$ (right).

V. Conclusion and perspectives

This paper presents the theoretical development of an exergy balance adapted to rotating frames of reference and its numerical application to the case of a propeller. The evolution of the exergy balance components is investigated for different operating regimes and boundary conditions, and figures of merit are introduced to characterize the efficiency of the system under study. Links can also be made between the exergy balance and classical efficiency curves, with supplementary information provided by the reversible efficiency that can theoretically be obtained. Phenomenological links are also made between physical phenomena and the exergy balance terms, which even allow to visualize regions of anergy generation and exergy outflow. There is still room for improvement for this formulation in terms of precision, in order to properly account for the residual of the exergy balance at the discrete level. For future works, a next step could also consist in implementing the relative velocity, relative frame formulation in FFX in order to compare the supplementary information that this balance would provide. Finally, an extension of the formulation to internal flows would allow to investigate more cases with configurations involving significant thermal exchanges and shockwaves. For example, in the case of a high-pressure compressor or turbine of an aircraft engine, thermal effects cannot be properly included in classical mechanical analyses. The exergy balance would then provide additional information on these

aspects and the physics involved in a single balance including both mechanical and thermal effects.

Appendix A: precision analysis

A.1. Numerical indicators of solution accuracy

In addition to physical analyses, the precision of the exergy balance should be discussed. If the estimation of the different terms of the exergy balance was perfect, the residual of Eq. (14) should be exactly zero. However, due to numerical dissipation linked to the turbulence model, the mesh and the numerical approximation of the different terms, this balance is not always respected at the discrete level. It is even more so in the case of an industrial grid, where mesh quality may be locally degraded in order to accommodate complex technological details or to reduce the number of points in flow regions that are not of primary interest.

Recently, numerical precision indicators have been investigated for this reason at ONERA. They consist in evaluating the error that is made in the energy conservation and the error made on the entropy equation at the discrete level, among others. Two such indicators are respectively denoted as E^* and $\dot{\mathcal{A}}^*$, with the corresponding expressions in the rotating reference frame formulation applied to the current propeller case being:

$$E^* = \int_{\partial\mathcal{V}} (\rho\delta E(\mathbf{V}' - \mathbf{s_e}') + p\mathbf{V}') \cdot \mathbf{n}' \, \mathrm{d}S \tag{21}$$

$$\dot{\mathcal{A}}^* = -T_\infty \int_{\partial\mathcal{V}} \rho\delta s(\mathbf{V}' - \mathbf{s_e}') \cdot \mathbf{n}' \, \mathrm{d}S + \int_{\mathcal{V}} \frac{T_\infty}{T^2} k(\nabla T)'^2 \, \mathrm{d}\mathcal{V} + \int_{\mathcal{V}} \frac{T_\infty}{T} \phi' \, \mathrm{d}\mathcal{V} + \int_{S_w} [\![T_\infty \rho\delta s(\mathbf{V}' - \mathbf{s_e}')]\!] \cdot \mathbf{n}' \, \mathrm{d}S \tag{22}$$

E^* allows to detect differences that may be associated to grid quality, insufficient convergence or numerical oscillations. $\dot{\mathcal{A}}^*$ is dominated by entropy generation through numerical dissipation. Naturally, the latter becomes significant downstream of aerodynamic bodies due to the dissipation of wakes and vortices by the numerical discretization and the turbulence model. The discrete error of the exergy balance equation can be expressed as $\dot{\mathcal{X}}^* = E^* - \dot{\mathcal{A}}^*$. As such, the numerically-balanced counterpart of Eq. (14) takes the following form:

$$\dot{\mathcal{X}}'_r = \underbrace{W\dot{\Gamma}' + \dot{\mathcal{X}}'_m + \dot{\mathcal{X}}'_{th} + \dot{\mathcal{A}}'_\phi + \dot{\mathcal{A}}'_{\nabla T} - \dot{\mathcal{X}}^*}_{RHSn} \tag{23}$$

While this balance is respected, it is stressed that it is not trivial to rigorously distinguish between the physical and the numerical effects in the total difference contained in $\dot{\mathcal{X}}^*$. For this reason, E^* and $\dot{\mathcal{A}}^*$ do not correspond to a correction but rather to an estimation of numerical errors in the analysis. Specific strategies have been developed in order to quantify and isolate these numerical errors, in particular the purely numerical anergy generation $\dot{A}_{sp}$ (also called

spurious anergy). This spurious anergy is equivalent to the difference between the anergy generated in the whole control volume and the anergy generated in the volumes associated to physical phenoma, here viscous and thermal volumes, which are detected using physical criteria [16].

A.2. Analysis for the nominal operating regime

A.2.1. Numerical precision indicators

The numerical precision is first investigated for the operating regime that is studied in section IV.C.1 with ω = 212.6 rad.s^{-1} and M_∞ = 0.3. The evolution of both E^*, $\dot{\mathcal{A}}^*$, $\dot{A}_{sp}$, and of the RHS, LHS (right-hand side and left-hand side of the exergy balance respectively), RHSn are plotted to make sure that the balance is respected.

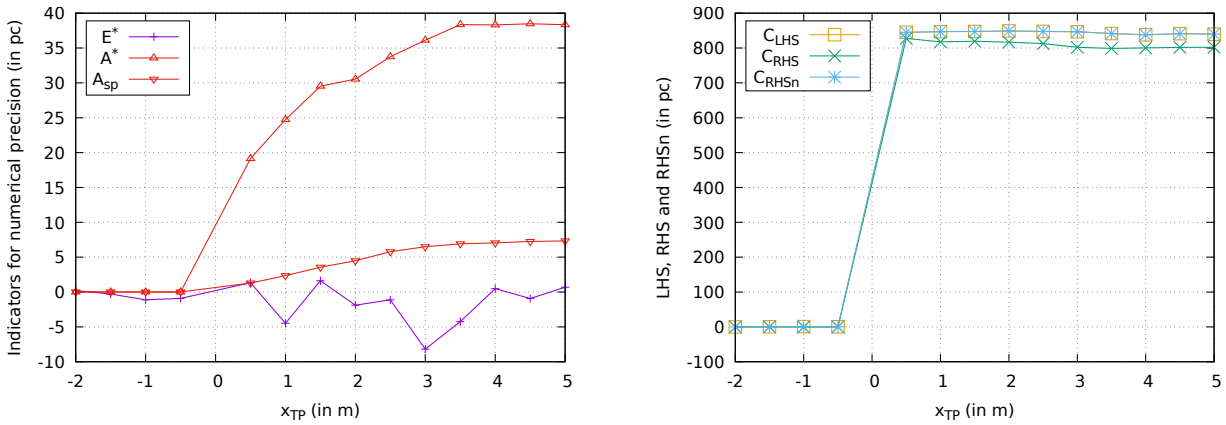

Fig. 21 Numerical error quantification for various downstream limits of the control volume.

Fig. 21 confirms that the inclusion of the $\dot{\mathcal{X}}^*$ term as in Eq. (23) leads to a balanced equation. E^* varies when moving the transverse plane downstream, but its absolute values remain within 5 power counts close to the propeller blade. Beyond roughly 2.5 meters, the grid is coarsened so the variations become more important. On the other hand, $\dot{\mathcal{A}}^*$ and $\dot{A}_{sp}$ are not significant unless the propeller is included inside the control volume. This is a result of numerical dissipation (numerical discretization and/or turbulence model) which naturally becomes even more significant further downstream. The spurious anergy calculated follows a similar trend as $\dot{\mathcal{A}}^*$ with lower values, highlighting that the numerical generation of anergy becomes more significant as the control volume is extended.

A.2.2. Precision of $\dot{\mathcal{X}}'_r$ and $W\dot{\Gamma}'$

$\dot{\mathcal{X}}'_r$ represents the shaft power transferred to the fluid and $W\dot{\Gamma}'$ its part converted into a power corresponding to the overall force projected on the x-axis (effective thrust in this case). The values obtained for these coefficients are thus compared with those of a near-field integration of forces done by elsA. The results are also compared to the near-field values of *ffd01* [3], another post-processing tool developed at ONERA allowing to perform a far-field drag breakdown

and which is also adapted to the case of a rotating reference frame [29, 30]. Table 3 shows the absolute values of the axial force C_{F_X} and torque power C_{T_X} obtained with the near-field elsA and *ffd01* analyses, compared with the near-field and far-field values obtained with FFX for $C_{W\dot{\Gamma}'}$ and $C_{\dot{\mathcal{X}}_r'}$. These absolute values and relative errors are computed for x_{TP} = 0.2m for the far-field integration, and only the parts of the walls for $x \leq 0.2$m are considered for the near-field one.

Software	elsA		*ffd01*		*FFX*			
Approach	near-field		near-field		near-field		far-field	
Variable	C_{F_X}	C_{T_X}	C_{F_X}	C_{T_X}	$C_{W\dot{\Gamma}'}$	$C_{\dot{\mathcal{X}}_r'}$	$C_{W\dot{\Gamma}'}$	$C_{\dot{\mathcal{X}}_r'}$
Absolute value (in counts)	733.05	847.08	734.15	846.29	734.31	846.28	733.47	846.67
Error relative to elsA near-field	0%	0%	0.15%	-0.09%	0.17%	-0.09%	0.06%	-0.05%

Table 3 Coefficient comparison for the partial domain analysis (x_{TP} = 0.2m).

Table 3 shows that the near-field values computed by *ffd01* are in very close agreement with the values computed by elsA. Part of the differences between these tools can be attributed to different methods used to reconstruct viscous fluxes on wall boundaries, but the results remain in good agreement. The values obtained with near-field computations performed by FFX show that $C_{\dot{\mathcal{X}}_r'}$ and $C_{W\dot{\Gamma}'}$ are also in good agreement with these results. The values obtained with far-field computations in *FFX* are fortuitously in better agreement with the results obtained with elsA as the relative error is close to 0.05% for both coefficients.

There exist several elements which may explain these differences between different software. A first source of inaccuracy may arise from the evaluation of $\mathbf{s_e}'$, since values used for the post-processing are cell-centered. In contrast to conservative variables which are part of the flow solution, $\mathbf{s_e}'$ is a direct function of the position vector, and can require a specific treatment for its evaluation in order to ensure the conservativity of its field at the discrete level [21]. A lack of precision is also to be expected for coarse parts of the mesh where the cell size is bigger, as can usually be observed as we approach the far-field boundary conditions. Another source for the difference between the near-field and far-field values in FFX could be coming from the trace of numerical dissipation of the scheme used in the numerical simulation. Finally, different integration methods are used in *FFX* compared to elsA and *ffd01*, which can also partly explain the differences observed. It should however be noted that the above results are in overall good agreement.

A.2.3. Sensitivity to the upstream and radial extension of the control volume

An additional study was carried out to investigate the exergy balance component sensitivity to control volume modifications, in directions where physical flow perturbations are expected to be small. For this purpose, the downstream limit of the control volume was fixed at $x_{TP} = 0.2m$. Then, for a fixed upstream limit of the control volume at

$x = -11.02$m, its outer limit radius was modified from $11.0m$ to $2.0m$ with a step of $1.0m$. Finally, with the radius limited at $r = 11.0$m, the control volume upstream limit was modified from $-11.0m$ to $-2.0m$ with a step of $1.0m$. This study was performed for the nominal operating regime, confirming a low sensitivity of the exergy balance components to these upstream and radial extensions. In particular, the relative variations of $\dot{\mathcal{X}}'_r, W\dot{\Gamma}', \dot{\mathcal{X}}'_m, \dot{\mathcal{X}}'_{th}$ and $\dot{\mathcal{A}}'_{tot}$ (with respect to values computed for the full control volume extending up to $x_{TP} = 0.2m$ downstream and up to the farfield boundary condition in the upstream and radial directions) were found to remain below 0.25%.

A.3. Analysis for different operating regimes

A.3.1 Numerical precision indicators

Similarly, the numerical precision indicators are plotted for the operating regimes explored in Sec. IV.C.4. The values are expressed in power counts and as a percentage of $\dot{\mathcal{X}}'_r$, with the absolute values plotted for the percentages of E^* and $\dot{\mathcal{X}}^*$ in order to better visualize their relative importance.

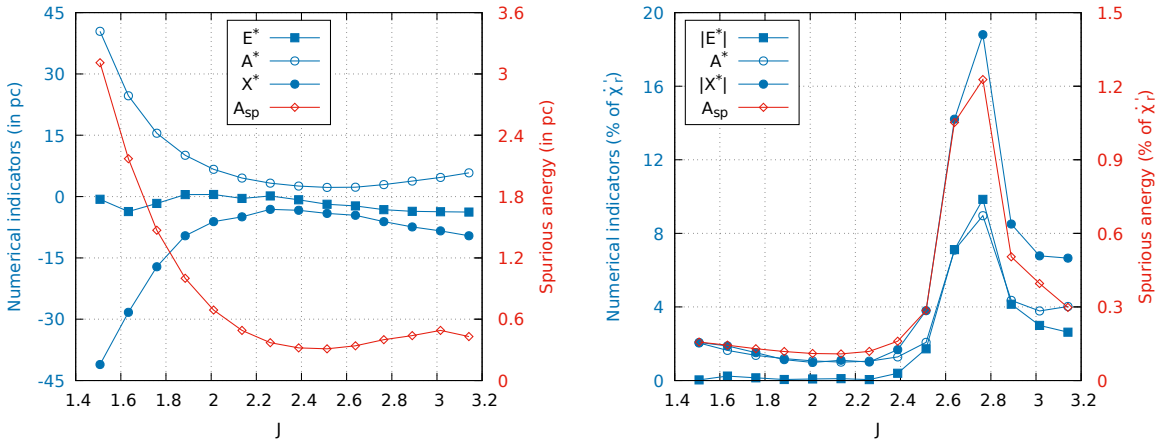

Fig. 22 E^*, $\dot{\mathcal{A}}^*$, $\dot{\mathcal{X}}^*$ **and** $\dot{A}_{sp}$ **evolution with J at** $x_{TP} = 0.2m$**.**

Fig. 22 shows that E^* remains at low values compared to levels attained by $\dot{\mathcal{A}}^*$, even when expressed as a percentage of $\dot{\mathcal{X}}'_r$ for $J \leq 2.4$. This indicates that most computations seem sufficiently converged and that the main impact on precision comes from numerical dissipation. For higher values of the advance ratio, E^* becomes comparable to $\dot{\mathcal{A}}^*$. This is likely because the convergence of the CFD computation for these operating regimes is less satisfactory and leads to more numerical imprecision inside the CFD solution itself. While the absolute values obtained for $\dot{\mathcal{A}}^*$ are much higher for lower J than for higher J, with a decreasing trend until $J = 2.51$ before it starts increasing again, relative values with respect to $\dot{\mathcal{X}}'_r$ are much more significant for higher J values. A peak proportional value is attained for E^*, $\dot{\mathcal{A}}^*$ and $\dot{A}_{sp}$ at $J = 2.76$, which could mean that this numerical solution gives the least satisfactory results in terms of precision among the different cases. It is however stressed that this peak also corresponds to the J values for which $\dot{\mathcal{X}}'_r \approx 0$, which could lead to artificially higher relative values for these indicators. The spurious anergy values follow a similar trend to

that of $\dot{\mathcal{A}}^*$ with lower values, showing that the purely numerical effects are also affected by the conditions used for the calculations.

1. A.3.2 $\dot{\mathcal{X}}'_r$ and $W\dot{\Gamma}'$ precision

In Sec. A.2, near-field and far-field values of $\dot{\mathcal{X}}'_r$ and $W\dot{\Gamma}'$ are compared to the values computed with elsA and *ffd01* in the case where the propeller functions in its nominal operating regime. A similar investigation is performed in this section to compare the values obtained with FFX for these coefficients to the ones computed by elsA for several operating regimes, as shown in Fig. 23. The associated figures of merit are also computed to estimate the impact of using the near-field or far-field expressions on the efficiency computed. The relative difference between FFX and elsA coefficients is computed as $\Delta\chi = \frac{\chi_{FFX} - \chi_{elsA}}{\chi_{elsA}}$

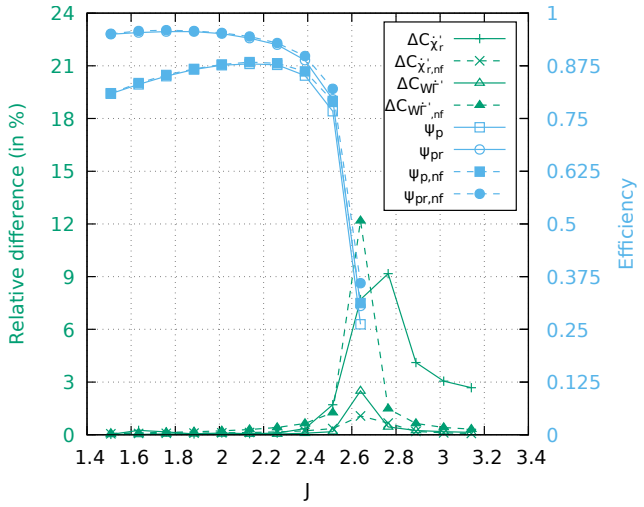

Fig. 23 Nearfield and farfield evolution of $\dot{\mathcal{X}}'_r$ and $W\dot{\Gamma}'$ with J with their corresponding efficiencies at $x_{TP} = 0.2m$.

Fig. 23 shows that the difference between the near-field and far-field values for these coefficients is not constant when the operating regime is modified. In the case of $W\dot{\Gamma}'$, the far-field expression is in better agreement than its near-field equivalent with the coefficients computed in elsA for all operating regimes. The maximum difference is obtained for J equal to 2.64, for which the relative difference obtained with the near-field expression is of approximately 17%, while the relative difference with the far-field expression is of almost 3%. For $\dot{\mathcal{X}}'_r$, the opposite behavior is observed with a better agreement obtained for the near-field expression computed with FFX. The biggest difference observed for the near-field computation of this term is again obtained for $J = 2.64$ and is equal to almost 3%, while a maximum of 9% is obtained for the far-field expression at $J = 2.76$. Again, it should be noted that $\dot{\mathcal{X}}'_r$ and $W\dot{\Gamma}'$ absolute values are very low for these operating regimes, potentially explaining the increase in relative difference at these J values. Furthermore, while most differences between the coefficients decrease for higher J values, $\Delta C_{\dot{\mathcal{X}}'_r}$ remains at a higher level for the maximum J values investigated. The differences between the near-field and far-field computations of these terms is also

visible on the evolution of ψ_p and ψ_{pr}. The efficiencies calculated using the far-field expressions are lower than the ones based on near-field calculations, with the highest differences being observed at the highest J values investigated.

A correlation is observed between the evolution of E^* in Fig. 22 and the results presented in Fig. 23. The most notable differences are obtained when peak values are reached by this numerical indicator, which shows that the differences observed can indeed be associated to the precision of the computation. The higher levels of relative difference for $\dot{\mathcal{X}}'_r$ at higher J values are also consistent with the evolution of E^* for these operating regimes. This is natural since these terms' expressions are linked to the energy balance.Overall, $W\dot{\Gamma}'_{,nf}$ and $\dot{\mathcal{X}}'_r$ seem to be the most sensitive expressions with respect to the accuracy of the numerical simulation.

Acknowledgments

The work presented in this paper was funded by the French Directorate General for Civil Aviation (DGAC) through the SUBLIME and IDEFFIX conventions. The studies presented have used the elsA software, whose development is partially funded by its three co-owners: ONERA, Airbus, SAFRAN. The authors would also like to thank Itham Salah el Din for providing the test case with the associated mesh for this study and Biel Ortun for his advice and knowledge.

References

[1] Banbury, J., Behrens, D., Bowell, Q., Campos, N., Cirilo, C., Choi, T. P., Dufresne, S., Hollingsworth, P., Markou, C., Mavris, D., Pinon, O., Raczynski, C., Roetger, T., Sung, W., and Toepoel, V. R., "The IATA technology roadmap report," *International Air Transport Association*, Vol. 3, 2009. URL `http://www.iata.org/SiteCollectionDocuments/Documents/Technology_Roadmap_May2009.pdf`.

[2] Advisory Council for Aviation Research and Innovation in Europe (ACARE), "Strategic Research and Innovation Agenda (SRIA)," . URL `https://www.acare4europe.org/wp-content/uploads/2022/02/Time_for_change_FlightPath_2050.pdf`, Accessed on 12th October 2022.

[3] van der Vooren, J., and Destarac, D., "Drag/thrust analysis of jet-propelled transonic transport aircraft: Definition of physical drag components," *Aerospace Science and Technology*, Vol. 8, No. 6, 2004, pp. 545–556. https://doi.org/10.1016/j.ast.2004.03.004.

[4] Destarac, D., "Far-Field / Near-Field Drag Balance and Applications of Drag Extraction in CFD," *CFD-Based Aircraft Drag Prediction and Reduction*, . VKI Lecture Series 2003, Von Karman Institute for Fluid Dynamics, Rhode Saint Genèse, February 3-7, 2003, National Institute of Aerospace, Hampton (VA), November 3-7, 2003.

[5] Bailly, D., Petropoulos, I., Wervaecke, C., Méheut, M., Atinault, O., and Fournis, C., "An Overview of ONERA Research Activities Related to Drag Analysis and Breakdown," *AIAA AVIATION 2021 FORUM*, American Institute of Aeronautics and Astronautics, 2021. https://doi.org/10.2514/6.2021-2551, AIAA Paper 2021-2551.

[6] Drela, M., "Considerations in Aerodynamic Force Decomposition," *AIAA AVIATION 2021 FORUM*, American Institute of Aeronautics and Astronautics, 2021. https://doi.org/10.2514/6.2021-2552, AIAA Paper 2021-2552.

[7] Drela, M., "Power Balance in Aerodynamic Flows," *AIAA Journal*, Vol. 47, No. 7, 2009, pp. 1761–1771. https://doi.org/10.2514/1.42409.

[8] Sanders, D. S., and Laskaridis, P., "Full-Aircraft Energy-Based Force Decomposition Applied to Boundary-Layer Ingestion," *AIAA Journal*, Vol. 58, No. 10, 2020, pp. 4357–4373. https://doi.org/10.2514/1.j058695.

[9] Uranga, A., Drela, M., Greitzer, E. M., Hall, D. K., Titchener, N. A., Lieu, M. K., Siu, N. M., Casses, C., Huang, A. C., Gatlin, G. M., and Hannon, J. A., "Boundary Layer Ingestion Benefit of the D8 Transport Aircraft," *AIAA Journal*, Vol. 55, No. 11, 2017, pp. 3693–3708. https://doi.org/10.2514/1.j055755.

[10] Uranga, A., Drela, M., Hall, D. K., and Greitzer, E. M., "Analysis of the Aerodynamic Benefit from Boundary Layer Ingestion for Transport Aircraft," *AIAA Journal*, Vol. 56, No. 11, 2018, pp. 4271–4281. https://doi.org/10.2514/1.j056781.

[11] Çengel, Y. A., and Boles, M. A., *Thermodynamics: An Engineering Approach.*, 2015. 8th edition, New York: McGraw-Hill.

[12] Moorhouse, D., Camberos, J., and Suchomel, C., "Entropy and Exergy Balance Equations for MHD Flow with Application to Hypersonic Vehicle Analysis and Design," *33rd Plasmadynamics and Lasers Conference*, American Institute of Aeronautics and Astronautics, 2002. https://doi.org/10.2514/6.2002-2183, AIAA Paper 2002-2183.

[13] Camberos, J., "On the Construction of Exergy Balance Equations for Availability Analysis," *8th AIAA/ASME Joint Thermophysics and Heat Transfer Conference*, American Institute of Aeronautics and Astronautics, 2002. https://doi.org/10.2514/6.2002-2880, AIAA Paper 2002-2880.

[14] Arntz, A., Atinault, O., and Merlen, A., "Exergy-Based Formulation for Aircraft Aeropropulsive Performance Assessment: Theoretical Development," *AIAA Journal*, Vol. 53, No. 6, 2015, pp. 1627–1639. https://doi.org/10.2514/1.j053467.

[15] Arntz, A., "Civil aircraft aero-thermo-propulsive performance assessment by an exergy analysis of high-fidelity CFD-RANS Flow Solutions," Ph.D. thesis, Lille 1 University - Sciences and Technologies, 2014. URL https://hal.archives-ouvertes.fr/tel-01113135.

[16] Petropoulos, I., Wervaecke, C., Bailly, D., and Derweduwen, T., "Numerical investigations of the exergy balance method for aerodynamic performance evaluation," *AIAA Aviation 2019 Forum*, American Institute of Aeronautics and Astronautics, 2019. https://doi.org/10.2514/6.2019-2926, AIAA Paper 2019-2926.

[17] Aguirre, M. Á., and Duplaa, S., "Exergetic Drag Characteristic Curves," *AIAA Journal*, Vol. 57, No. 7, 2019, pp. 2746–2757. https://doi.org/10.2514/1.j057985.

[18] Aguirre, M. Á., Duplaa, S., Carbonneau, X., and Turnbull, A., "Velocity Decomposition Method for Exergy-Based Drag Prediction," *AIAA Journal*, Vol. 58, No. 11, 2020, pp. 4686–4701. https://doi.org/10.2514/1.j059414.

[19] Aguirre, M. Á., "Exergy analysis of innovative aircraft with aeropropulsive coupling," Ph.D. thesis, 2022. URL http://www.theses.fr/2022ESAE0008.

[20] Fiore, M., "Influence of cavity flow on turbine aerodynamics," Ph.D. thesis, ISAE-Institut Supérieur de l'Aéronautique et de l'Espace, 2019. URL http://www.theses.fr/2019ESAE0013.

[21] Boniface, J. C., "Calcul d'écoulements compressibles autour de rotors d'hélicoptères en vol stationnaire ou en vol d'avancement par résolution des équations d'Euler," Ph.D. thesis, ENSAM, 1995. URL http://www.theses.fr/1995ENAM0037.

[22] Kozuch, L., "Etude de l'écoulement dans une turbomachine axiale transsonique en présence ou non d'une distorsion amont : Validation d'un outil de simulation et analyse instationnaire," Ph.D. thesis, Ecole centrale de Lyon, 2002. URL https://bibli.ec-lyon.fr/exl-doc/TH_T1890_lkozuch.pdf.

[23] Meheut, M., "Multidisciplinary Adjoint-based Optimizations in the MADELEINE Project: Overview and Main Results," *AIAA AVIATION 2021 FORUM*, American Institute of Aeronautics and Astronautics, 2021. https://doi.org/10.2514/6.2021-3052, AIAA Paper 2021-3052.

[24] Ortun, B., "A coupled RANS/lifting-line analysis for modelling the aerodynamics of distributed propulsion," *AHS Aeromechanics & Design for Transformative Vertical Flight*, 2018.

[25] Fischer, J.-S., and Ortun, B., "Simulation & Analysis of the Aerodynamic Interactions between Distributed Propellers and Wings," *AHS Aeromechanics & Design for Transformative Vertical Flight*, 2018.

[26] Cambier, L., Heib, S., and Plot, S., "The Onera elsA CFD software: input from research and feedback from industry," *Mechanics & Industry*, Vol. 14, No. 3, 2013, pp. 159–174. https://doi.org/10.1051/meca/2013056.

[27] Benoit, C., Péron, S., and Landier, S., "Cassiopee: A CFD pre- and post-processing tool," *Aerospace Science and Technology*, Vol. 45, 2015, pp. 272–283. https://doi.org/10.1016/j.ast.2015.05.023.

[28] Lovely, D., and Haimes, R., "Shock detection from computational fluid dynamics results," *14th Computational Fluid Dynamics Conference*, American Institute of Aeronautics and Astronautics, 1999. https://doi.org/10.2514/6.1999-3285, AIAA Paper 1999-3285.

[29] Verley, S., "Evaluation du couple 'champ lointain' d'un rotor d'hélicoptère en vol stationnaire : analyse de résultats issus de simulations numériques de mécanique des fluides," Ph.D. thesis, Université d'Orléans, 2012. URL http://www.theses.fr/2012ORLE2087.

[30] Meheut, M., "Thrust and Torque Far-field Analysis of Propeller and Counter Rotating Open Rotor Configurations," *31st AIAA Applied Aerodynamics Conference*, American Institute of Aeronautics and Astronautics, 2013. https://doi.org/10.2514/6.2013-2803, AIAA Paper 2013-2803.